Geophysical Journal International

Geophys. J. Int. (2016) **207,** 89–110
Advance Access publication 2016 July 14
GJI Gravity, geodesy and tides

doi: 10.1093/gji/ggw257

Elastic tidal response of a laterally heterogeneous planet: a complete perturbation formulation

Chuan Qin, Shijie Zhong and John Wahr

Department of Physics, University of Colorado at Boulder, Boulder, CO 80309*, USA. E-mail: chuan.qin@colorado.edu*

Accepted 2016 July 8. Received 2016 July 8; in original form 2016 April 2

SUMMARY

Constraining laterally varying structures in planetary interiors is important for understanding both the composition and the internal dynamics of a planet. Recognizing that seismic imaging technique is currently only viable for studying the Earth's interior structures, methods that can be supported by advanced space geodetic techniques may become alternatives to 'image' the interiors of other planets. The method of tidal tomography is one possibility, and it relies on high precision measurement of the response of a planet to its body tide. However, it is essential to develop an efficient analytical tool that computes the dependence of tidal response to 3-D interior structures. In this paper, we present a complete formulation of such an analytical tool, which calculates to high accuracy the tidal response of a terrestrial planet with lateral heterogeneities in its elastic and density structures. We treat the lateral heterogeneities as small perturbations and derive the governing equations based on the perturbation theory. In a spherical harmonic representation, equations at each order of perturbation are reduced into multiple matrix equations at harmonics that are allowed by mode couplings, and the total response equals the sum of all those single-harmonic responses, which can be solved semi-analytically. We test our perturbation method by applying it to the Moon with a harmonic degree-1 mantle structure for which the perturbation solutions of the tidal response are compared with those from a fully numerical method. The remarkable agreement between results from these two methods validates the perturbation method. As an example, we then use the perturbation method to evaluate the impact of lunar crustal thickness variations on tidal response of the Moon. We find that lunar crust produces much smaller degree-3 tidal responses than a relatively weak degree-1 structure in the deep lunar mantle. Our calculations show that degree-3 tidal response measurements may hold key constraints on possible degree-1 mantle structure of the Moon, as suggested from previous modelling results.

Key words: Time variable gravity; Lunar and planetary geodesy and gravity; Tides and planetary waves; Dynamics of lithosphere and mantle; Planetary interiors.

1 INTRODUCTION

Space observations over the past decades have revealed that some planetary bodies in the solar system have apparent long-wavelength laterally varying features at their surfaces. For example, the Earth's moon displays global asymmetries in its surface chemical compositions, mare basalt volcanism and crustal thickness (e.g. Zuber *et al*. 1994; Smith *et al*. 1997; Lawrence *et al*. 1998; Tompkins & Pieters 1999; Lawrence *et al*. 2002). Mars shows significant differences in crustal thickness between northern and southern hemispheres and in volcanism between eastern and western hemispheres (Zuber 2001). Mercury is proved to have a magnetic field in a north-south asymmetry, for which the surface magnetic field at the northern hemisphere is about three times stronger than that at the southern hemisphere (e.g. Anderson *et al*. 2011). The Saturn's moon Enceladus features a geologically older northern hemisphere and a younger southern hemisphere, where an active geyser system with abnormally high surface temperature is observed at the south-pole region (e.g. Porco *et al*. 2006; Spencer *et al*. 2006). It has been proposed that these laterally varying features originate from the deep interiors of these planetary bodies (e.g. Zhong *et al*. 2000; Laneuville *et al*. 2013). Therefore, imaging the interior structures and constraining the interior material properties are crucial for understanding the current state and the dynamic evolution of these bodies. However, high-resolution imaging of the planetary interiors relies on a global network of seismometers, which are unavailable on any of the planetary bodies other than the Earth.

Advanced space geodetic techniques may provide alternative and cost-effective tools to infer the interior structure of a planetary body. The GRACE mission used a twin-satellite system to capture very small variations in the Earth's gravity field, by measuring the position of the

orbiting satellites and the relative ranging rate between them at extremely high precision (Tapley *et al*. 2004). The later lunar mission GRAIL launched a similar pair of twin satellites to the Moon's low-altitude orbit and measured the Moon's gravity field and its time-variations to an unprecedented precision (Zuber *et al*. 2013). The onboard LOLA (Lunar Orbiter Laser Altimeter) instrument on LRO (Lunar Reconnaissance Orbiter) can determine the lunar global topography at high resolution and precision, and may potentially capture small ground movement of the lunar surface (Smith *et al*. 2010). These measurements and future missions open a window for using the response of a planet (i.e. changes in gravitational potential and/or surface topography) to time-varying body tide to constrain 3-D long-wavelength structure of the planetary interior, that is, tidal tomography (e.g. Latychev *et al*. 2009; Zhong *et al*. 2012). Tidal force acting on a planetary body with 3-D interior structures excites additional response modes that are distinct from those for a spherically symmetric body (1-D). In principle, the elastic response of a planetary body has the identical frequency as the applied time-varying tidal force, and thus is spectrally separable from the static response and other low frequency responses. Although none of the above missions has so far been targeted to extract small tidal response signals for inference of possible 3-D interior structures, an analytical tool that can effectively compute the tidal response of a planetary body with 3-D interior structures is desirable.

Additionally, such an analytical tool would help improve the theoretical framework in solving general geophysical response problems. The theory and method for solving the elastic tidal/loading response of a spherically symmetric (i.e. 1-D) planetary body were established long ago (Longman 1962; Longman 1963; Farrell 1972). In the following decades, response problems for a planetary body with laterally heterogeneous material properties (i.e. 3-D) could only be solved through fully numerical methods (e.g. Latychev *et al*. 2009; Zhong *et al*. 2012). Until recently, stimulated by the more advanced geodetic measurements, two different analytical tools in solving 3-D tidal response problems have been developed. First, motivated by the GRAIL mission, we developed a semi-analytical perturbation method based on the Love number formalism that solves the elastic tidal response of a planetary body with lateral heterogeneity in the shear modulus (Qin *et al*. 2014). Second, Lau *et al*. (2015) developed a new normal mode theory that can predict the tidal response of a laterally heterogeneous, rotating and anelastic Earth in the semi-diurnal band. Their goal is to use GPS measurements of ground deformation to constrain the Earth's deep mantle structure. In Qin *et al*. (2014), we took the advantage of mathematical simplicity of the perturbation theory, and extended our formulation to the second order of perturbation for high accuracy. Systematic benchmark tests were made by comparing the perturbation solutions with those from a finite element code (Zhong *et al*. 2003; A *et al*. 2013), showing remarkable agreement between these two solutions. However, Qin *et al*. (2014) only considered lateral heterogeneity in the shear modulus in their formulation and did not include lateral heterogeneities in other properties such as the first Lamé parameter and the density. The benchmark calculations were only made for radial displacement and gravitational potential in the response (Qin *et al*. 2014).

This study is a continuation of our previous work (Qin *et al*. 2014). Here, we present a complete perturbation method by incorporating lateral heterogeneities in the elastic and density structures into one formulation. Benchmarks are performed to validate our perturbation method, which are done not only for response in radial displacement and gravitational potential but also for that in horizontal displacement. The paper is organized as follows. In Section 2, we derive the governing equations and the perturbation formulation. A special treatment in dealing with nonzero net force on the system that can potentially be caused by density anomaly is demonstrated. In Section 3, we transform our perturbation equations into a matrix form through spherical harmonic (SH) and vector spherical harmonic (VSH) expansions, and present solution method for solving the equations. In Section 4, we present benchmark results of tidal responses of a hemispherically asymmetric (degree-1) Moon that are computed from our perturbation method and a finite element based numerical method. We then use the perturbation method to calculate the tidal response of the Moon caused by the large crustal thickness variations that are inferred from the GRAIL observations. The final section is on conclusions and discussions.

2 THEORY

We seek to derive governing equations for tidal response of a spherically stratified planetary body superposed with small lateral heterogeneities in its rocky mantle and crust (hereafter, we refer to 'mantle' as both mantle and crust). The mantle is assumed to be compressible and respond to time-varying tidal force elastically with self-gravitational effect. We include all sources of lateral heterogeneities, which can exist in the two elastic moduli (shear modulus μ and first Lamé parameter λ) and the density ρ. The equation of motion originates from the conservation of momentum, which is given as (Dahlen & Tromp 1998; Tromp & Mitrovica 1999b)

$$\nabla \cdot \mathbf{T}^{\mathrm{E}} - \rho^{\mathrm{E}} \nabla \phi^{\mathrm{E}} = 0, \tag{1}$$

where ρ^{E}, ϕ^{E} and $\mathbf{T}^{\mathrm{E}}$ are Eulerian density, gravitational potential and stress field, respectively.

2.1 Background state

A spherically symmetric (1-D) planetary body is in hydrostatic equilibrium and has no deformation without external force being applied. From eq. (1), we have

$$\nabla \cdot \mathbf{T}_0 = \rho_0 \nabla \phi_0, \tag{2}$$

where ρ_0, ϕ_0 and $\mathbf{T}_0$ ($\mathbf{T}_0 = -p_0\mathbf{I}$ and p_0 is the hydrostatic pressure) are the reference density profile, the gravitational potential and the stress field, respectively, and are all functions of radius. ϕ_0 satisfies the Poisson's equation

$$\nabla^2\phi_0 = 4\pi G\rho_0. \tag{3}$$

When there exist small lateral heterogeneities, $\delta\mu_0$, $\delta\lambda_0$ and $\delta\rho_0$ ($\delta\mu_0/\mu_0 \ll 1$, $\delta\lambda_0/\lambda_0 \ll 1$ and $\delta\rho_0/\rho_0 \ll 1$, where μ_0, λ_0 and ρ_0 are 1-D profiles of the shear modulus μ, the first Lamé parameter λ and the density ρ, respectively), although $\delta\mu_0$ and $\delta\lambda_0$ alone have no direct effect, the density anomaly $\delta\rho_0$ would act as a body force in causing a pre-stressed system involving mantle deformation. As a result, this pre-stressed system forms a new background state, which can be described by a new equation of motion, as

$$\nabla\cdot\mathbf{T}_0' - \rho_0'\nabla\phi_0' = 0, \tag{4}$$

where $\rho_0' = \rho_0 + \delta\rho_0$, $\phi_0' = \phi_0 + \delta\phi_0$, $\mathbf{T}_0' = -p_0\mathbf{I}+\boldsymbol{\tau}_0$, respectively, $\boldsymbol{\tau}_0$ is the stress induced by the body force (i.e. the pre-stress), $\delta\phi_0$ is the change in gravitational potential due to $\delta\rho_0$.

It is important to note that the density-induced potential change $\delta\phi_0$ can no longer be determined from the Poisson's equation $\nabla^2\delta\phi_0 = 4\pi G\delta\rho_0$ alone, it also contains the effect from undulations (i.e. dynamic topography) of any density interfaces in the mantle that are caused by $\delta\rho_0$ (e.g. Hager & Richards 1989). More generally, eq. (4) can be used to describe a system that is pre-stressed by a combined effect from not only internal density anomaly $\delta\rho_0$ but also different other sources, such as static body tide, rotation, surface loading and etc., as long as they act in entirely different frequency bands from that of the body tide we consider. However, solving eq. (4) for a pre-stressed state may require a viscous or viscoelastic rheology for the mantle, because such a flow deformation operates at a much longer time scale than the elastic tidal deformation that we consider in this study. Consequently, we ignore any pre-stress effect.

2.2 Net force due to density anomaly

The time-varying body tide may be induced by the orbital eccentricity or obliquity of the planetary body. For example, Mercury's tide is almost solely contributed by the Sun, and its time-dependent part is mainly caused by its orbital eccentricity. Body tide in the moons of the gas giants is predominantly raised by their planets, while the effect from the Sun and other planets is negligible. For the Earth's Moon, the tidal potential from the Sun is ~200 times smaller than that due to the Earth, and thus is excluded from our analyses. Also, we only consider the leading terms in the Moon's tidal potential that is caused by its eccentric orbit in our analyses, that is, the harmonic degree-2 terms. We denote the tidal potential as $V_{\rm td}(t)$ or $V_{\rm td}(\boldsymbol{r}, t)$, so that the tidal force can be expressed as $-\rho_0'\nabla V_{\rm td}(t)$. Since $V_{\rm td}(t)$ is at degree-2 SHs, the response of a spherically symmetric (1-D) body would be at the same harmonics. However, when coupled with laterally heterogeneous (3-D) structures, the degree-2 tidal force also excites non-degree-2 harmonics in the response.

In principle, solving tidal response of a planetary body requires external forces be balanced, which means the net external force on the system must be equal to zero. On a spherically symmetric (1-D) body, the tidal force $-\rho_0\nabla V_{\rm td}(t)$ never causes a net force. However, when density anomaly $\delta\rho_0$ is present, the coupling term $-\delta\rho_0\nabla V_{\rm td}(t)$ may result in a nonzero net force on the planetary body. Physically, this net force would only accelerate the planetary body but not cause any deformation. However, keeping this net force in the term $-\delta\rho_0\nabla V_{\rm td}(t)$ and including it in the equation of motion would impose an incorrect force balance on the system, leading to errors in the solutions. To correctly solve the tidal response, we remove this net force component by redefining the problem in a non-inertial reference frame which is accelerating with the planetary body. A fictitious inertial force is added in the equation of motion as to cancel the net force, as discussed below.

Mode coupling in the forcing term $-\delta\rho_0\nabla V_{\rm td}(t)$ can be solved by VSH expansion that will be introduced in Section 3. In the expansion form,

$$-\delta\rho_0\nabla V_{\rm td}(t) = \sum_{l,m}\boldsymbol{f}_{l,m}(\boldsymbol{r}, t), \tag{5}$$

where $\boldsymbol{f}_{l,m}(\boldsymbol{r}, t)$ is the modal component at harmonic (l, m). It can be mathematically proved that only a harmonic degree-1 modal component can cause a nonzero net force. We thus focus on the degree-1 components in eq. (5), which can be further expressed as

$$\boldsymbol{f}_{1,m}(\boldsymbol{r}, t) = f^P_{1,m}(r, t)\boldsymbol{P}_{1,m} + f^B_{1,m}(r, t)\boldsymbol{B}_{1,m}, \tag{6}$$

where $\boldsymbol{P}_{1,m}$ and $\boldsymbol{B}_{1,m}$ are VSH basis functions for a spheroidal vector (see Section 3) of degree 1 and order m of 1, 0 or -1, and $f^P_{1,m}$ and $f^B_{1,m}$ are the expansion coefficients for corresponding basis functions. We compute the net force $\boldsymbol{f}_{\rm net}(t)$ by integrating $\boldsymbol{f}_{1,m}(\boldsymbol{r}, t)$ throughout the mantle, as

$$\boldsymbol{f}_{\rm net}(t) = \iiint_V \boldsymbol{f}_{1,m}(\boldsymbol{r}, t)r^2\sin\theta\,\mathrm{d}r\,\mathrm{d}\theta\,\mathrm{d}\phi. \tag{7}$$

The direction of $\boldsymbol{f}_{\rm net}(t)$ depends on the choice of m and

$$\boldsymbol{f}_{\rm net}(t) = \begin{cases} f_0(t)\hat{\boldsymbol{x}} & m = 1 \\ f_0(t)\hat{\boldsymbol{y}} & m = -1\,, \\ f_0(t)\hat{\boldsymbol{z}} & m = 0 \end{cases} \tag{8}$$

where $\hat{\boldsymbol{x}}$, $\hat{\boldsymbol{y}}$ and $\hat{\boldsymbol{z}}$ are unit vectors in Cartesian coordinates, and

$$f_0(t) = \frac{4\pi}{3} \int_{r_{\rm cmb}}^{a} \left[f^P_{1,m}(r,t) + 2 f^B_{1,m}(r,t) \right] r^2 \, {\rm d}r, \tag{9}$$

where $r_{\rm cmb}$ and a are the radii of the core–mantle boundary (CMB) and the surface, respectively. $\boldsymbol{f}_{\rm net}(t)$ would accelerate the planet with the acceleration

$$\boldsymbol{a}_{\rm tot}(t) = \frac{\boldsymbol{f}_{\rm net}(t)}{M}, \tag{10}$$

where M is the total mass of the planet.

Solving degree-1 deformation in the accelerating reference requires an inertial force be added to every portion of the mantle, where the inertial force is equal to

$$\boldsymbol{f}_{\rm int}(\boldsymbol{r},t) = -\rho_0' \boldsymbol{a}_{\rm tot}(t) = -\rho_0' \frac{f_0(t)}{M} (\boldsymbol{P}_{1,m} + \boldsymbol{B}_{1,m}), \tag{11}$$

which is in the opposite direction of the acceleration. Here we make use of the following relation in eq. (11).

$$\boldsymbol{P}_{1,m} + \boldsymbol{B}_{1,m} = \begin{cases} \hat{\boldsymbol{x}} & m = 1 \\ \hat{\boldsymbol{y}} & m = -1 \\ \hat{\boldsymbol{z}} & m = 0 \end{cases}. \tag{12}$$

2.3 Governing equations

The time-varying tidal force $-\rho_0{}' \nabla V_{\rm td}(t)$ deforms the pre-stressed mantle elastically further by $\boldsymbol{u}(t)$, in addition to any background deformation. As a result, the equation of motion is updated to

$$\nabla \cdot [\mathbf{T}_0' + \mathbf{T}^{\rm E1}(t)] - [\rho_0' + \rho^{\rm E1}(t)] \nabla [\phi_0' + V_{\rm td}(t) + \varphi^{\rm E1}(t)] - \rho_0' \boldsymbol{a}_{\rm tot}(t) = 0, \tag{13}$$

where $\rho^{\rm E1}(t)$, $\varphi^{\rm E1}(t)$ and $\mathbf{T}^{\rm E1}(t)$ are Eulerian perturbations in density, gravitational potential and stress, respectively, due to the incremental deformation $\boldsymbol{u}(t)$, and the inertial force $\boldsymbol{f}_{\rm int} = -\rho_0' \boldsymbol{a}_{\rm tot}$ is added to cancel potential nonzero net force on the planet. Subtracting eq. (4) (i.e. the background state) from eq. (13) and neglecting small terms involving products of Eulerian increments lead to the linearized governing equation for tidal response, which is given by

$$\nabla \cdot \mathbf{T}^{\rm E1}(t) - \rho_0' \nabla [V_{\rm td}(t) + \varphi^{\rm E1}(t)] - \rho^{\rm E1}(t) \nabla \phi_0' - \rho_0' \boldsymbol{a}_{\rm tot}(t) = 0. \tag{14}$$

Note that we have ignored the effect of pre-stress $\boldsymbol{\tau}_0$ for linearization of eq. (14) as usually done in formulation for similar analyses (e.g. Dahlen & Tromp 1998; Tromp & Mitrovica 1999a). Considering $\delta\phi_0 \ll \phi_0$, we will also neglect the effect of $\delta\phi_0$ in eq. (14).

We substitute the Eulerian incremental stress $\mathbf{T}^{\rm E1}(t)$ with the Lagrangian form through the relation (Dahlen & Tromp 1998)

$$\mathbf{T}^{\rm E1}(t) = \mathbf{T}^{\rm L1}(t) - \boldsymbol{u}(t) \cdot \nabla \mathbf{T}_0, \tag{15}$$

where $\mathbf{T}^{\rm L1}(t)$ can be related to $\boldsymbol{u}(t)$ through the constitutive relation by assuming simple elasticity for the mantle, as

$$\mathbf{T}^{\rm L1} = \mathbf{T}^{\rm L1}(\lambda_0', \mu_0', \boldsymbol{u}) = \lambda_0' (\nabla \cdot \boldsymbol{u}) \mathbf{I} + \mu_0' (\nabla \boldsymbol{u} + \nabla^{\rm T} \boldsymbol{u}), \tag{16}$$

where $\mu_0' = \mu_0 + \delta\mu_0$ and $\lambda_0' = \lambda_0 + \delta\lambda_0$. We obtain the final equation of motion as

$$\nabla \cdot \mathbf{T}^{\rm L1}(\lambda_0', \mu_0', \boldsymbol{u}) - \nabla(\rho_0 \boldsymbol{u} \cdot \nabla \phi_0) - \rho_0' \nabla (V_{\rm td} + \varphi^{\rm E1}) - \rho^{\rm E1} \nabla \phi_0 - \rho_0' \boldsymbol{a}_{\rm tot} = 0, \tag{17}$$

and together with the Poisson's equation

$$\nabla^2 \varphi^{\rm E1} = 4\pi G \rho^{\rm E1}, \tag{18}$$

where the Eulerian density perturbation $\rho^{\rm E1}$ is related to $\boldsymbol{u}$ through

$$\rho^{\rm E1} = -\nabla \cdot (\rho_0' \boldsymbol{u}). \tag{19}$$

Note that $\boldsymbol{u}$, $\varphi^{\rm E1}$, $\mathbf{T}^{\rm L1}$ and $\boldsymbol{a}_{\rm tot}$ all have the same time dependence as the tidal potential $V_{\rm td}(t)$. Here, we can omit the time dependence in eqs (16)–(19) for elastic response.

Compared with the governing equations in Qin *et al*. (2014), eqs (16)–(19) also include the effects of $\delta\lambda_0$ and $\delta\rho_0$ on the response, together with that of $\delta\mu_0$. If $\delta\mu_0$, $\delta\lambda_0$ and $\delta\rho_0$ vanish, eqs (16)–(19) would automatically reduce to the 1-D equations that reconcile eqs (1)–(3) in Qin *et al*. (2014). Hereafter, we omit any superscripts that denote an Eulerian or Lagrangian quantity.

2.4 Perturbation formulation

Solving eqs (16)–(19) for $\boldsymbol{u}$ and φ fully determines the tidal response. We solve the equations using a perturbation method, in which we treat any small lateral heterogeneities (3-D) in the mantle as perturbations to the 1-D reference state (similar to what Qin *et al*. (2014) used in modelling 3-D structures in shear modulus μ). We denote the tidal response solution for the 1-D reference structure as $(\boldsymbol{u}_0, \varphi_0)$ and the solution for that being perturbed by a 3-D structure as $(\boldsymbol{u}, \varphi)$. The difference between the two solutions, denoted as $(\boldsymbol{u}', \varphi')$[i.e. $(\boldsymbol{u}', \varphi') = (\boldsymbol{u}, \varphi) - (\boldsymbol{u}_0, \varphi_0)$], represents the incremental tidal response as a result of the 3-D structure. Taking $(\boldsymbol{u}_0, \varphi_0)$ as zeroth order solution, we further divide $(\boldsymbol{u}', \varphi')$ into high order solutions by the order of perturbation in the lateral heterogeneities to represent incremental responses at different levels of accuracy, as $(\boldsymbol{u}', \varphi') = (\boldsymbol{u}_1, \varphi_1) + (\boldsymbol{u}_2, \varphi_2) + (\boldsymbol{u}'', \varphi'')$, where $(\boldsymbol{u}_1, \varphi_1)$, $(\boldsymbol{u}_2, \varphi_2)$ and $(\boldsymbol{u}'', \varphi'')$ are called first order, second order and residual (higher than second order) solutions, respectively (Qin *et al*. 2014). Since a second order approximation to $(\boldsymbol{u}, \varphi)$ is sufficiently accurate, we drop $(\boldsymbol{u}'', \varphi'')$ and replace $\boldsymbol{u}$ and φ in eqs (16)–(19) with $\boldsymbol{u}_0 + \boldsymbol{u}_1 + \boldsymbol{u}_2$ and $\varphi_0 + \varphi_1 + \varphi_2$, respectively. As a result, different orders of solutions (up to second order of perturbation) are grouped into individual sets of perturbation equations, which can be expressed in a generalized form as

$$\nabla \cdot \mathbf{T}_D - \nabla(\rho_0 \boldsymbol{u}_D \cdot \nabla\phi_0) - \rho_0 \nabla\varphi_D + \nabla \cdot (\rho_0 \boldsymbol{u}_D)\nabla\phi_0 = -\boldsymbol{\mathcal{F}}_D, \tag{20}$$

$$\nabla^2 \varphi_D + 4\pi G \nabla \cdot (\rho_0 \boldsymbol{u}_D) = -\mathcal{G}_D, \tag{21}$$

$$\mathbf{T}_D = \lambda_0(\nabla \cdot \boldsymbol{u}_D)\mathbf{I} + \mu_0(\nabla \boldsymbol{u}_D + \nabla^{\mathrm{T}} \boldsymbol{u}_D), \tag{22}$$

where $\boldsymbol{\mathcal{F}}_D$ and $\mathcal{G}_D$ are called the coupling terms, the subscript D indicates the order of perturbation and can be 0, 1 or 2, that is, the zeroth, first or second order. Eqs (20)–(22) have non-trivial solutions only when the coupling term $\boldsymbol{\mathcal{F}}_D$ or $\mathcal{G}_D$ is non-zero.

When $D = 0$ (i.e. zeroth order), $\boldsymbol{\mathcal{F}}_0 = -\rho_0 \nabla V_{\mathrm{td}}$ and $\mathcal{G}_0 = 0$, and eqs (20)–(22) solves the tidal response for a spherically symmetric (1-D) body. The technique in solving 1-D response was well developed decades ago (Longman 1962; Longman 1963; Farrell 1972). Difficulties lie in solving the higher order equations, that is for $D = 1$ or 2, due to involvement of the coupling terms. At higher orders, $\boldsymbol{\mathcal{F}}_D = \boldsymbol{\mathcal{F}}_D^{\mu} + \boldsymbol{\mathcal{F}}_D^{\lambda} + \boldsymbol{\mathcal{F}}_D^{\rho}$, where $\boldsymbol{\mathcal{F}}_D^{\mu}$, $\boldsymbol{\mathcal{F}}_D^{\lambda}$ and $\boldsymbol{\mathcal{F}}_D^{\rho}$ are mutually independent and are contributions to $\boldsymbol{\mathcal{F}}_D$ from the coupling between the lower order $(D-1)$ solution and the lateral heterogeneities $\delta\mu_0$, $\delta\lambda_0$ and $\delta\rho_0$, respectively, as seen from

$$\boldsymbol{\mathcal{F}}_D^{\mu} = \nabla \cdot \left[\delta\mu_0(\nabla \boldsymbol{u}_{D-1} + \nabla^{\mathrm{T}} \boldsymbol{u}_{D-1})\right], \tag{23}$$

$$\boldsymbol{\mathcal{F}}_D^{\lambda} = \nabla(\delta\lambda_0 \nabla \cdot \boldsymbol{u}_{D-1}), \tag{24}$$

$$\boldsymbol{\mathcal{F}}_D^{\rho} = -\delta\rho_0 \nabla\varphi_{D-1} + \nabla \cdot (\delta\rho_0 \boldsymbol{u}_{D-1})\nabla\phi_0 + \boldsymbol{f}_D^{\rho}. \tag{25}$$

Note that $\boldsymbol{\mathcal{F}}_D^{\mu}$ and $\boldsymbol{\mathcal{F}}_D^{\lambda}$ keep the same form in different orders of equations, while $\boldsymbol{\mathcal{F}}_D^{\rho}$ differs by an extra term $\boldsymbol{f}_D^{\rho}$ between the first and the second orders. Specifically,

$$\boldsymbol{f}_1^{\rho} = -\delta\rho_0 \nabla V_{\mathrm{td}} - \rho_0 \boldsymbol{a}_{\mathrm{tot}}, \tag{26}$$

$$\boldsymbol{f}_2^{\rho} = -\delta\rho_0 \boldsymbol{a}_{\mathrm{tot}}. \tag{27}$$

Also, at higher orders,

$$\mathcal{G}_D = 4\pi G \nabla \cdot (\delta\rho_0 \boldsymbol{u}_{D-1}), \tag{28}$$

and $\mathcal{G}_D$ is non-zero only when $\delta\rho_0 \neq 0$.

Solving eqs (20)–(22) requires appropriate continuity conditions as well as boundary conditions at the outer surface and the CMB (e.g. Qin *et al*. 2014). Across any concentric interface in the spherically layered mantle, $\boldsymbol{u}_D$, φ_D, the normal traction term $(\hat{r} \cdot \mathbf{T}_D + \boldsymbol{\mathcal{B}}_D)$ and the potential gradient term $[\hat{r} \cdot (\nabla\varphi_D + 4\pi G\rho_0 \boldsymbol{u}_D) + \mathcal{H}_D]$ must be continuous, which can be expressed as

$$[\boldsymbol{u}_D]_-^+ = [\varphi_D]_-^+ = \left[\hat{r} \cdot \mathbf{T}_D + \boldsymbol{\mathcal{B}}_D\right]_-^+ = \left[\hat{r} \cdot (\nabla\varphi_D + 4\pi G\rho_0 \boldsymbol{u}_D) + \mathcal{H}_D\right]_-^+ = 0, \tag{29}$$

where $[]_-^+$ symbolizes the jump of the enclosed quantity across an interface, $\hat{r}$ is the normal vector in the radial direction, $\boldsymbol{\mathcal{B}}_D$ and $\mathcal{H}_D$ are two other coupling terms. Specifically, $\boldsymbol{\mathcal{B}}_D$ is induced by $\delta\mu_0$ or $\delta\lambda_0$ while $\mathcal{H}_D$ results from $\delta\rho_0$, and both of them are non-zero only in the higher order equations (i.e. $D = 1$ or 2). Splitting $\boldsymbol{\mathcal{B}}_D$ into terms that represent $\delta\mu_0$ and $\delta\lambda_0$ contributions, as $\boldsymbol{\mathcal{B}}_D = \boldsymbol{\mathcal{B}}_D^{\mu} + \boldsymbol{\mathcal{B}}_D^{\lambda}$, $\boldsymbol{\mathcal{B}}_D^{\mu}$, $\boldsymbol{\mathcal{B}}_D^{\lambda}$ and $\mathcal{H}_D$ are given by

$$\boldsymbol{\mathcal{B}}_D^{\mu} = \hat{r} \cdot \left[\delta\mu_0(\nabla \boldsymbol{u}_{D-1} + \nabla^{\mathrm{T}} \boldsymbol{u}_{D-1})\right], \tag{30}$$

$$\boldsymbol{\mathcal{B}}_D^{\lambda} = \hat{r} \cdot [\delta\lambda_0(\nabla \cdot \boldsymbol{u}_{D-1})\mathbf{I}], \tag{31}$$

$$\mathcal{H}_D = \hat{r} \cdot 4\pi G\delta\rho_0 \boldsymbol{u}_{D-1}, \tag{32}$$

respectively. The surface and CMB boundary conditions are provided in the next section in a matrix form.

3 METHOD

We solve the perturbation equations, that is eqs (20)–(22), through a two-step procedure (Qin *et al*. 2014). Step one: we perform SH and VSH expansions, respectively, for any 3-D scalars and vectors that enter in the perturbation equations. In this way, a complete set of harmonic modes in the tidal response solution can be pre-determined by solving the mode coupling terms. Meanwhile, any radially dependent component of the solution is separated from the angular dependence in the harmonics, thus reducing the problem of solving the partial differential equations (i.e. eqs 20–22) into solving multiple sets of ordinary differential equations (ODEs) with respect to the radius that are associated with the harmonics allowed by the mode couplings. Each set of ODEs can then be converted into a more manageable matrix form for solution (Dahlen & Tromp 1998; Tromp & Mitrovica 1999b). Step two: we adopt the propagator matrix method to solve those resulting matrix equations for each response mode from each order of perturbation. The total response is equal to the sum of all those responses.

Eqs (20)–(22) and the corresponding continuity and boundary conditions are non-dimensionalized by the following scalings:

$$r = a\tilde{r},\ \boldsymbol{u}_D = a\tilde{\boldsymbol{u}}_D,\ \varphi_D = 4\pi G\rho_{\rm cmb}a^2\tilde{\varphi}_D,\ \nabla = \frac{1}{a}\tilde{\nabla},$$

$$\mu_0 = \mu_{\rm cmb}\tilde{\mu}_0,\ \lambda_0 = \mu_{\rm cmb}\tilde{\lambda}_0,\ \rho_0 = \rho_{\rm cmb}\tilde{\rho}_0,$$

$$\delta\mu_0 = \mu_{\rm cmb}\delta\tilde{\mu}_0,\ \delta\lambda_0 = \mu_{\rm cmb}\delta\tilde{\lambda}_0,\ \delta\rho_0 = \rho_{\rm cmb}\delta\tilde{\rho}_0,$$

$$\mathbf{T}_D = \mu_{\rm cmb}\tilde{\mathbf{T}}_D,\ \boldsymbol{\mathcal{F}}_D = \frac{\mu_{\rm cmb}}{a}\tilde{\boldsymbol{\mathcal{F}}}_D,\ \mathcal{B}_D = \mu_{\rm cmb}\tilde{\boldsymbol{\mathcal{B}}}_D,$$

$$\mathcal{G}_D = 4\pi G\rho_{\rm cmb}\tilde{\mathcal{G}}_D,\ \mathcal{H}_D = 4\pi G\rho_{\rm cmb}a\tilde{\mathcal{H}}_D, \tag{33}$$

where the tilt denotes a non-dimensional quantity, a is the radius of the planet, $\rho_{\rm cmb}$ and $\mu_{\rm cmb}$ are the reference density and shear modulus right above the CMB, respectively. Thus, the non-dimensional form of the perturbation equations [i.e. eqs (20)–(22)] and the associated continuity conditions [eq. (29)] are expressed as

$$\tilde{\nabla}\cdot\tilde{\mathbf{T}}_D - \eta\left[\tilde{\nabla}(\tilde{\rho}_0\tilde{\boldsymbol{u}}_D\cdot\tilde{\nabla}\tilde{\phi}_0) + \tilde{\rho}_0\tilde{\nabla}\tilde{\varphi}_D - \tilde{\nabla}\cdot(\tilde{\rho}_0\tilde{\boldsymbol{u}}_D)\tilde{\nabla}\tilde{\phi}_0\right] = -\tilde{\boldsymbol{\mathcal{F}}}_D, \tag{34}$$

$$\tilde{\nabla}^2\tilde{\varphi}_D + \tilde{\nabla}\cdot(\tilde{\rho}_0\tilde{\boldsymbol{u}}_D) = -\tilde{\mathcal{G}}_D, \tag{35}$$

$$\tilde{\mathbf{T}}_D = \tilde{\lambda}_0(\tilde{\nabla}\cdot\tilde{\boldsymbol{u}}_D)\mathbf{I} + \tilde{\mu}_0(\tilde{\nabla}\tilde{\boldsymbol{u}}_D + \tilde{\nabla}^{\rm T}\tilde{\boldsymbol{u}}_D), \tag{36}$$

$$[\tilde{\boldsymbol{u}}_D]^+_- = [\tilde{\varphi}_D]^+_- = \left[\hat{r}\cdot\tilde{\mathbf{T}}_D + \tilde{\boldsymbol{\mathcal{B}}}_D\right]^+_- = \left[\hat{r}\cdot(\tilde{\nabla}\tilde{\varphi}_D + \tilde{\rho}_0\tilde{\boldsymbol{u}}_D) + \tilde{\mathcal{H}}_D\right]^+_- = 0, \tag{37}$$

respectively, where $\eta = \frac{4\pi G\rho_{\rm cmb}^2a^2}{\mu_{\rm cmb}}$, $\tilde{\boldsymbol{\mathcal{F}}}_D = \tilde{\boldsymbol{\mathcal{F}}}^{\mu}_D + \tilde{\boldsymbol{\mathcal{F}}}^{\lambda}_D + \eta\tilde{\boldsymbol{\mathcal{F}}}^{\rho}_D$ and $\tilde{\boldsymbol{\mathcal{B}}}_D = \tilde{\boldsymbol{\mathcal{B}}}^{\mu}_D + \tilde{\boldsymbol{\mathcal{B}}}^{\lambda}_D$. Hereafter, all the quantities are non-dimensional and we omit the tilts for brevity.

We expand all 3-D scalar and vector variables in the spherical coordinates (r, θ, ϕ) into SHs and VSHs, respectively, of which the basis functions are (Dahlen & Tromp 1998; Tromp & Mitrovica 1999b)

$$Y_{lm} = Y_{lm}(\theta,\phi),\ \boldsymbol{P}_{lm} = \hat{r}Y_{lm},\ \boldsymbol{B}_{lm} = \nabla_1 Y_{lm},\ \boldsymbol{C}_{lm} = \hat{r}\times\nabla_1 Y_{lm}, \tag{38}$$

where Y_{lm} is the SH function in real form, $\boldsymbol{P}_{lm}$, $\boldsymbol{B}_{lm}$ and $\boldsymbol{C}_{lm}$ are vector functions defined over (θ, ϕ), l and m are harmonic degree and order, respectively, which define a unique mode in the harmonics. The explicit expressions of these basis functions are given in appendix A of Qin *et al*. (2014). Assuming that the lateral heterogeneities are composed of eigenstructures of different SHs, they can be expanded into

$$\delta\mu_0 = \sum_{l_1,m_1}\Delta^{\mu}_{l_1m_1}(r)\mu_0(r)Y_{l_1m_1}(\theta,\phi), \tag{39}$$

$$\delta\lambda_0 = \sum_{l_1,m_1}\Delta^{\lambda}_{l_1m_1}(r)\lambda_0(r)Y_{l_1m_1}(\theta,\phi), \tag{40}$$

$$\delta\rho_0 = \sum_{l_1,m_1}\Delta^{\rho}_{l_1m_1}(r)\rho_0(r)Y_{l_1m_1}(\theta,\phi), \tag{41}$$

respectively, where $\Delta_{l_1m_1}(r)$ measures the lateral variability of the heterogeneities and is considered to be small.

$\boldsymbol{u}_D$, φ_D and $\hat{r}\cdot\mathbf{T}_D$ are expanded respectively into (Dahlen & Tromp 1998; Tromp & Mitrovica 1999b)

$$\boldsymbol{u}_D = \sum_{l,m}\left(U^D_{lm}\boldsymbol{P}_{lm} + V^D_{lm}\boldsymbol{B}_{lm} + W^D_{lm}\boldsymbol{C}_{lm}\right), \tag{42}$$

$$\varphi_D = \sum_{l,m}K^D_{lm}Y_{lm}, \tag{43}$$

$$\hat{r}\cdot\mathbf{T}_D = \sum_{l,m}\left(R^D_{lm}\boldsymbol{P}_{lm} + S^D_{lm}\boldsymbol{B}_{lm} + T^D_{lm}\boldsymbol{C}_{lm}\right), \tag{44}$$

where the expansion coefficients are functions of radius. The expansion coefficients U_{lm}^D, V_{lm}^D, W_{lm}^D and K_{lm}^D fully describe the tidal response solution at mode (l, m) and order D. R_{lm}^D, S_{lm}^D, T_{lm}^D and an auxiliary variable Q_{lm}^D are derivative terms, which are given specifically by (Dahlen & Tromp 1998; Tromp & Mitrovica 1999b)

$$R_{lm}^D = (\lambda_0 + 2\mu_0)\dot{U}_{lm}^D + \frac{\lambda_0}{r}\left(2U_{lm}^D - l(l+1)V_{lm}^D\right), \tag{45}$$

$$S_{lm}^D = \mu_0\left(\dot{V}_{lm}^D - \frac{V_{lm}^D}{r} + \frac{U_{lm}^D}{r}\right), \tag{46}$$

$$T_{lm}^D = \mu_0\left(\dot{W}_{lm}^D - \frac{W_{lm}^D}{r}\right), \tag{47}$$

$$Q_{lm}^D = \dot{K}_{lm}^D + \frac{l+1}{r}K_{lm}^D + \rho_0 U_{lm}^D, \tag{48}$$

where a dot denotes the first order derivative with respect to radius.

The mode coupling terms $\boldsymbol{\mathcal{F}}_D$, $\mathcal{G}_D$, $\boldsymbol{\mathcal{B}}_D$ and $\mathcal{H}_D$ (for $D > 0$) need to be expanded into appropriate forms in order for the high-order responses to be solved. Here, we only show the symbolic expansion forms of these terms, as

$$\boldsymbol{\mathcal{F}}_D = \sum_{l,m}\left(F_{lm}^{p,D}\boldsymbol{P}_{lm} + F_{lm}^{b,D}\boldsymbol{B}_{lm} + F_{lm}^{c,D}\boldsymbol{C}_{lm}\right), \tag{49}$$

$$\mathcal{G}_D = \sum_{l,m} G_{lm}^D Y_{lm}, \tag{50}$$

$$\boldsymbol{\mathcal{B}}_D = \sum_{l,m}\left(B_{lm}^{p,D}\boldsymbol{P}_{lm} + B_{lm}^{b,D}\boldsymbol{B}_{lm} + B_{lm}^{c,D}\boldsymbol{C}_{lm}\right), \tag{51}$$

$$\mathcal{H}_D = \sum_{l,m} H_{lm}^D Y_{lm}, \tag{52}$$

where $D = 1$ or 2, while their full expressions are given in Appendix A and will enter in the matrix equations before the propagator matrix method being applied. Note that determining the coupling terms at order D requires that the response at order $D-1$ be fully solved. The coupling terms govern the response modes at each order of perturbation (for $D > 0$) through the selection rule [eq. (22) in Qin *et al.* (2014)]. A permissible mode in the response is indicated by a non-trivial set of expansion coefficients of $\boldsymbol{\mathcal{F}}_D$, $\boldsymbol{\mathcal{B}}_D$, $\mathcal{H}_D$ and $\mathcal{G}_D$ at that specific mode. Thus, tidal response is restricted to a finite number of pre-determined modes other than spans in infinite number of modes. More descriptions of the mode coupling can be referred to section 3.2 of Qin *et al.* (2014).

The SH and VSH expansion forms (i.e. eqs 39–52) help turn the perturbation equations at order D (eqs 20–22) into equations for individual response modes, and these equations can be further reduced to ODEs with respect to radius by dropping angular dependence in the harmonics. The ODEs of a single mode belong to either one of the two categories: spheroidal (s) and toroidal (t), which describe two non-overlapping sets of components in the response. The spheroidal (s) component includes all the vector components that span in $\boldsymbol{P}_{lm}$ and $\boldsymbol{B}_{lm}$, and potential and potential derivatives; the toroidal component only includes vector components in $\boldsymbol{C}_{lm}$. We can convert these ODEs into a matrix form, and the spheroidal and toroidal equations share the same general form, as

$$\frac{\mathrm{d}\boldsymbol{X}_{lm}^D}{\mathrm{d}r} = \mathbf{A}_l\boldsymbol{X}_{lm}^D - \boldsymbol{F}_{lm}^D, \tag{53}$$

where $\boldsymbol{X}_{lm}^D$ is the solution vector of mode (l, m), $\mathbf{A}_l$ is a square matrix and depends on l but not on m or D, and $\boldsymbol{F}_{lm}^D$ is the vectorized form of the two coupling terms $\boldsymbol{\mathcal{F}}_D$ and $\mathcal{G}_D$. The explicit forms of $\boldsymbol{X}_{lm}^D$, $\mathbf{A}_l$ and $\boldsymbol{F}_{lm}^D$ as well as the associated continuity and boundary conditions are different for spheroidal and toroidal modes. Specifically,

(1) Spheroidal mode

$$\boldsymbol{X}_{lm}^D = \left(U_{lm}^D, V_{lm}^D, R_{lm}^D, S_{lm}^D, K_{lm}^D, Q_{lm}^D\right)^T. \tag{54}$$

$$\mathbf{A}_l = \begin{pmatrix} -\frac{2\lambda_0}{r\beta} & \frac{l(l+1)\lambda_0}{r\beta} & \frac{1}{\beta} & 0 & 0 & 0 \\ -\frac{1}{r} & \frac{1}{r} & 0 & \frac{1}{\mu_0} & 0 & 0 \\ \frac{4}{r}(\frac{\gamma}{r} - \xi) & -\frac{l(l+1)}{r}(\frac{2\gamma}{r} - \xi) & -\frac{4\mu_0}{r\beta} & \frac{l(l+1)}{r} & -\frac{\xi(l+1)}{g_0 r} & \frac{\xi}{g_0} \\ \frac{1}{r}(\xi - \frac{2\gamma}{r}) & -\frac{1}{r^2}\left[2\mu_0 - l(l+1)(\gamma + \mu_0)\right] & -\frac{\lambda_0}{r\beta} & -\frac{3}{r} & \frac{\xi}{r g_0} & 0 \\ -\rho_0 & 0 & 0 & 0 & -\frac{l+1}{r} & 1 \\ -\rho_0\frac{l+1}{r} & \rho_0\frac{l(l+1)}{r} & 0 & 0 & 0 & \frac{l-1}{r} \end{pmatrix}, \tag{55}$$

where $\beta = \lambda_0 + 2\mu_0$, $\gamma = \frac{\mu_0(3\lambda_0+2\mu_0)}{\lambda_0+2\mu_0}$, $\xi = \eta\rho_0 g_0$ and $\eta = \frac{4\pi G\rho_{\rm cmb}^2 a^2}{\mu_{\rm cmb}}$.

$$\boldsymbol{F}_{lm}^{D} = \left(0, 0, F_{lm}^{p,D}, F_{lm}^{b,D}, 0, G_{lm}^{D}\right)^{\rm T}. \tag{56}$$

The vectorized continuity conditions in the solid mantle and the boundary conditions are, respectively,

$$\left[U_{lm}^{D}\right]_{-}^{+} = \left[V_{lm}^{D}\right]_{-}^{+} = \left[K_{lm}^{D}\right]_{-}^{+} = \left[R_{lm}^{D} + B_{lm}^{p,D}\right]_{-}^{+} = \left[S_{lm}^{D} + B_{lm}^{b,D}\right]_{-}^{+} = \left[Q_{lm}^{D} + H_{lm}^{D}\right]_{-}^{+} = 0, \tag{57}$$

$$\boldsymbol{X}_{lm}^{D}(r_{\rm cmb}) = \left(U_{lm}^{D}, V_{lm}^{D}, \eta\rho_0\left(K_{lm}^{D}+g_0 U_{lm}^{D}\right), 0, K_{lm}^{D}, \frac{2l+1}{r_{\rm c}}K_{lm}^{D} + \rho_0 U_{lm}^{D}\right)^{T}_{r=r_{\rm cmb}}, \tag{58}$$

$$\boldsymbol{X}_{lm}^{D}(a) = (U_{lm}^{D}, V_{lm}^{D}, 0, 0, K_{lm}^{D}, 0)^{T}_{r=a}, \tag{59}$$

where $\boldsymbol{X}_{lm}^{D}(r_{\rm cmb})$ and $\boldsymbol{X}_{lm}^{D}(a)$ are solution vectors at the CMB and the outer surface, respectively.

(2) Toroidal mode

$$\boldsymbol{X}_{lm}^{D} = \left(W_{lm}^{D}, T_{lm}^{D}\right)^{T}. \tag{60}$$

$$\mathbf{A}_l = \begin{pmatrix} \frac{1}{r} & \frac{1}{\mu_0} \\ \frac{(l+2)(l-1)\mu_0}{r^2} & -\frac{3}{r} \end{pmatrix}. \tag{61}$$

$$\boldsymbol{F}_{lm}^{D} = \left(0, F_{lm}^{c,D}\right)^{T}. \tag{62}$$

The associated continuity conditions and boundary conditions are

$$\left[W_{lm}^{D}\right]_{-}^{+} = \left[T_{lm}^{D} + B_{lm}^{c,D}\right]_{-}^{+} = 0, \tag{63}$$

$$\boldsymbol{X}_{lm}^{D}(r_{\rm cmb}) = \left(W_{lm}^{D}, 0\right)^{T}_{r=r_{\rm cmb}}, \tag{64}$$

$$\boldsymbol{X}_{lm}^{D}(a) = \left(W_{lm}^{D}, 0\right)^{T}_{r=a}, \tag{65}$$

respectively.

Solving eqs (16)–(19) for the total tidal response $(\boldsymbol{u}, \varphi)$, up to second order accuracy in the perturbation, is now equivalent to summing over the responses of all the individual modes at every order of perturbation. The relative magnitude of the response is only a function of the lateral variabilities in the heterogeneities (see Appendix A). In addition, response at each mode is a combined effect of the three sources of lateral heterogeneities (i.e. those in μ, λ and ρ). As a direct consequence of our perturbation formulation, the first order response is simply the sum of the first order responses induced by individual sources, that is, only one source of lateral heterogeneity appears while the other two are zeroed out. This can be shown as

$$\boldsymbol{X}_{lm}^{1} = \boldsymbol{X}_{lm}^{1,\mu} + \boldsymbol{X}_{lm}^{1,\lambda} + \boldsymbol{X}_{lm}^{1,\rho}, \tag{66}$$

where $\boldsymbol{X}_{lm}^{1,\mu}$, $\boldsymbol{X}_{lm}^{1,\lambda}$ and $\boldsymbol{X}_{lm}^{1,\rho}$ ($\boldsymbol{X}_{lm}^{2,\mu}$, $\boldsymbol{X}_{lm}^{2,\lambda}$ and $\boldsymbol{X}_{lm}^{2,\rho}$ for later) are first order (second order) solutions due to lateral heterogeneity only in μ, λ and ρ, respectively. This summation rule, however, does not hold for the second order responses. The first order solution $\boldsymbol{X}_{lm}^{1}$ would enter in the second order coupling terms (see eqs 23–28 and 30–32), resulting in $\boldsymbol{X}_{lm}^{2,\mu}$, $\boldsymbol{X}_{lm}^{2,\lambda}$, $\boldsymbol{X}_{lm}^{2,\rho}$ as well as cross effects between the lateral heterogeneities into the second order solution $\boldsymbol{X}_{lm}^{2}$, as

$$\boldsymbol{X}_{lm}^{2} = \boldsymbol{X}_{lm}^{2,\mu} + \boldsymbol{X}_{lm}^{2,\lambda} + \boldsymbol{X}_{lm}^{2,\rho} + \left(\boldsymbol{\chi}_{lm}^{\delta\mu\otimes\delta\lambda} + \boldsymbol{\chi}_{lm}^{\delta\mu\otimes\delta\rho} + \boldsymbol{\chi}_{lm}^{\delta\lambda\otimes\delta\rho}\right), \tag{67}$$

where the symbol $\otimes$ represents the cross effects between two lateral heterogeneities.

We implement the propagator matrix method based on a fourth order Runge–Kutta numerical scheme to solve the whole set of matrix equations, mode by mode, from zeroth to second order of perturbation. The implementation of the propagator matrix method can be referred to section 3.3 and appendix C in Qin *et al*. (2014). The whole solution procedure of the perturbation method is summarized in Appendix B.

4 RESULTS

In this section, we use the perturbation method to calculate the tidal response of a laterally heterogeneous planetary body. As we did in our previous study (Qin *et al*. 2014), we continue to apply our method to the Earth's moon, of which the long-wavelength structure in depth is still unknown. But compared to other planetary bodies, we have a much better constraint on the Moon's 1-D reference profile (Weber *et al*. 2011) as well as its 3-D structure at shallow depths, for example, lunar crustal thickness variations (e.g. Wieczorek *et al*. 2013).

The Moon has a clear hemispherical asymmetry in its surface geological settings, for example, mare volcanism (e.g. Wieczorek *et al*. 2006) and crustal thickness (e.g. Wieczorek *et al*. 2013). Those asymmetries may have originated from a deeper source of long-wavelength heterogeneities, from a dynamic point of view (e.g. Zhong *et al*. 2000; Laneuville *et al*. 2013). More interestingly, recent analyses on deep seismicity in the lunar interior (Nakamura 2005) imply that those potential heterogeneities may have partially survived the thermochemical evolution and remain in the present-day lunar mantle (Qin *et al*. 2012). One mechanism predicts that those potential mantle heterogeneities, if existed, may have the same asymmetric distribution as that near the surface, which is a nearside-farside antipodal distribution (Qin *et al*. 2012). This mantle structure can be described predominantly by a (1, 1) SH in certain depth range in our chosen coordinate system (i.e. the origin of the coordinate system is fixed at the centre of the Moon, with x-axis pointing towards the sub-Earth point and z-axis perpendicular to the Moon's orbital plane). Considering such (1, 1) structure in the elastic moduli and the density, we have

$$\delta\mu_0 = \Delta^{\mu}_{1,1}(r)\mu_0(r)Y_{1,1} = -\delta^{\mu}_{1,1}(r)\mu_0(r)\sin\theta\cos\phi, \tag{68}$$

$$\delta\lambda_0 = \Delta^{\lambda}_{1,1}(r)\lambda_0(r)Y_{1,1} = -\delta^{\lambda}_{1,1}(r)\lambda_0(r)\sin\theta\cos\phi, \tag{69}$$

$$\delta\rho_0 = \Delta^{\rho}_{1,1}(r)\rho_0(r)Y_{1,1} = -\delta^{\rho}_{1,1}(r)\rho_0(r)\sin\theta\cos\phi, \tag{70}$$

where $Y_{1,1} = -\sqrt{\frac{3}{4\pi}}\sin\theta\cos\phi$, $\Delta_{1,1}$ is called the lateral variability, $\delta_{1,1}$ measures the amplitude of the (1, 1) lateral variability and $\delta_{1,1} = \sqrt{\frac{3}{4\pi}}\Delta_{1,1}$. In general, $\Delta_{1,1}(r)$ is piecewise constant as a function of the radius.

In the following calculations, we select the time-varying part of the tidal potential that is due to the eccentricity of the Moon's orbit, and only consider the leading harmonic degree-2 terms [Wahr *et al*. 2009; eq. (4) in Qin *et al*. (2014)]. In a simplified form, the tidal potential is given by

$$V_{\rm td}(\boldsymbol{r}, t) = \left[\Phi_{2,0}(r)Y_{2,0} + \Phi_{2,2}(r)Y_{2,2}\right]T(t), \tag{71}$$

which contains both (2, 0) and (2, 2) components. $T(t)$ represents the time dependence of the tidal potential, which can be dropped when solving elastic tidal response.

For a 1-D planetary body, tidal response can be fully described by three non-dimensional Love numbers (Love 1911). The tidal response is spheroidal and the solution (i.e. for $D = 0$) can be expressed by

$$\begin{bmatrix} U^0_{l_0m_0}(r) \\ V^0_{l_0m_0}(r) \\ K^0_{l_0m_0}(r) \end{bmatrix} = \Phi^{\rm td}_{l_0m_0}(r) \begin{bmatrix} h_{l_0}(r)/g_0 \\ l_{l_0}(r)/g_0 \\ k_{l_0}(r) \end{bmatrix}, \tag{72}$$

where (l_0, m_0) denotes the harmonic of a specific potential term, h_{l_0}, l_{l_0} and k_{l_0} are tidal Love numbers, which represent responses in radial displacement, horizontal displacement and gravitational potential, respectively. The Love numbers depend only on the 1-D reference profile and the harmonic degree (Love 1911; Farrell 1972). For a planetary body with 3-D structure, additional (high order) responses due to the mode coupling occur at multiple harmonics (l, m)'s in either spheroidal or toroidal mode. For each mode at order of perturbation D, we non-dimensionalize the tidal response solution based on eq. (72), and normalize it further by the three Love numbers. As a result, we get

$$h^{D'}_{lm}(r) = \frac{U^D_{lm}(r)}{U^0_{l_0m_0}(r)}, \quad l^{D'}_{lm}(r) = \frac{V^D_{lm}(r)}{V^0_{l_0m_0}(r)}, \quad k^{D'}_{lm}(r) = \frac{K^D_{lm}(r)}{K^0_{l_0m_0}(r)}, \quad w^{D'}_{lm}(r) = \frac{W^D_{lm}(r)}{V^0_{l_0m_0}(r)}, \tag{73}$$

where $h^{D'}_{lm}$, $l^{D'}_{lm}$ and $k^{D'}_{lm}$ ($w^{D'}_{lm}$) are called relative responses of a spheroidal (toroidal) mode $s^D(l, m)$ [$t^D(l, m)$]. Note that $h^{D'}_{lm}$, $l^{D'}_{lm}$, $k^{D'}_{lm}$ and $w^{D'}_{lm}$ can be positive or negative values. At the zeroth order, $h^{0'}_{l_0m_0} = l^{0'}_{l_0m_0} = k^{0'}_{l_0m_0} \equiv 1$, and $w^{0'}_{l_0m_0}$ does not exist.

We now use our perturbation method to do the following calculations. First, we run benchmark calculations to verify the formulation and implementation of the perturbation method for lateral heterogeneities in elastic structures, similar to the benchmark cases in Qin *et al*. (2014) (see table 1 in Qin *et al*. (2014) for the 1-D reference model of the Moon). The benchmark is done by comparing solutions from our perturbation method with those from a finite element method (Zhong *et al*. 2012; A *et al*. 2013; Qin *et al*. 2014). Second, since the finite element solutions are not yet available for cases with lateral heterogeneity in density, we calculate the density effect on the tidal response and compare it with the effect from lateral heterogeneity in shear modulus. Third, we evaluate the impact of lunar crustal thickness variations on the tidal response.

4.1 Benchmarks

In Qin *et al*. (2014), benchmarks were performed for cases in which (1, 1) lateral heterogeneity exists purely in the shear modulus μ. Here, we first apply the same procedure on (1, 1) lateral heterogeneity in first Lamé parameter λ, by comparing the tidal response solutions from the perturbation method and the finite element method (Zhong *et al*. 2003; A *et al*. 2013). For benchmark purposes, the responses to (2, 0) and (2, 2) tidal forcing components are computed separately, such that the relative magnitude of the forcing needs not to be considered. Also for simplicity, we set the amplitudes of lateral variability in elastic and density structures, that is, $\delta^{\mu}_{1,1}$, $\delta^{\lambda}_{1,1}$ and $\delta^{\rho}_{1,1}$, to be constant throughout the lunar mantle (i.e. independent of the radius).

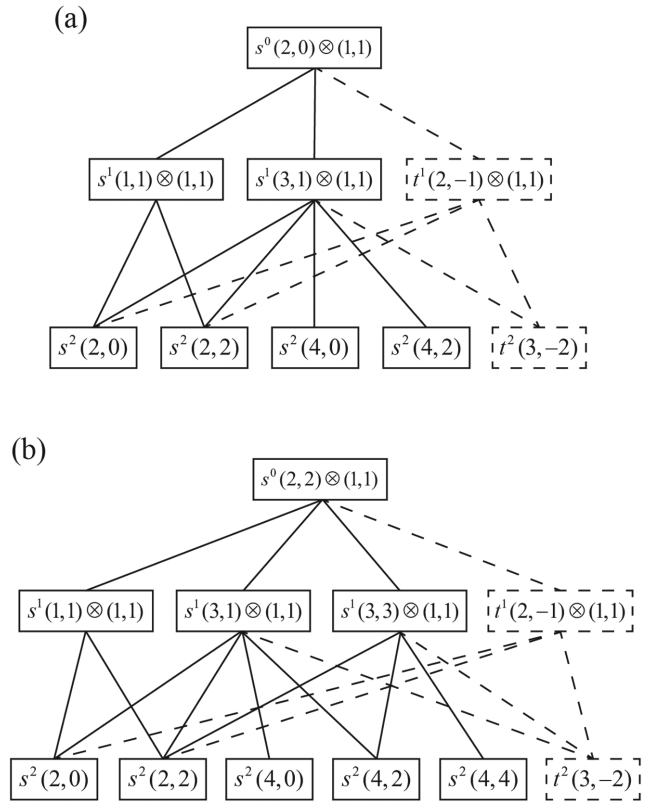

Figure 1. Hierarchies of mode couplings (up to order of perturbation $D = 2$) between spherical harmonic (1, 1) lateral heterogeneity in shear modulus μ, first Lamé parameter λ or density ρ and (2, 0) (a) and (2, 2) (b) tidal forcing, respectively. s or t denotes a spheroidal or toroidal mode, and superscript 0, 1 or 2 denotes order of perturbation D. The dashed boxes and lines mark the toroidal modes and the couplings that are associated with toroidal modes, respectively, which are allowed in μ and ρ cases but prohibited in λ case.

We first show the mode coupling diagrams to the second order of perturbation for (2, 0) and (2, 2) tidal forcing in Figs 1(a) and (b), respectively. The selection rule [eq. (22) in Qin *et al*. (2014)] holds the same for $\delta\mu_0$, $\delta\lambda_0$ and $\delta\rho_0$, except that $\delta\lambda_0$ does not induce any toroidal modes as $\delta\mu_0$ and $\delta\rho_0$ do. This said, we obtain the same set of spheroidal modes in the response from different sources of (1, 1) lateral heterogeneity, but the toroidal modes $t^1(2, -1)$ and $t^2(3, -2)$ and the mode couplings that are associated with them (marked by dashed frames and lines in Fig. 1) do not exist for $\delta\lambda_0$ case.

Fig. 2 shows the absolute values of the relative tidal responses of all the spheroidal modes in response to (2, 0) and (2, 2) tidal forcing for cases with different amounts of lateral variability in λ, computed from both the perturbation method and the finite element method. The lateral variability $\delta^{\lambda}_{1,1}$ is varied from 2.5 to 40 per cent, and nine different values are picked in this range for finite element calculations. The lunar mantle shell is divided into 12×48^3 elements in the finite element models. SH expansion is done for the grid-based numerical solutions, such that the expansion coefficients can be directly compared with the perturbation solutions. The top and bottom panels of Fig. 2 show the tidal responses to (2, 0) and (2, 2) tidal forcing, respectively. For both force components, the left and right panels show the relative responses in surface radial displacement (i.e. $|h^{D'}_{lm}(a)|$) and incremental gravitational potential (i.e. $|k^{D'}_{lm}(a)|$), respectively. Fig. 2 shows a remarkably good agreement between the results from the two different methods for the $\delta\lambda_0$ case (also Table 1). All the significant modes from the finite element calculations are exactly the first and the second order spheroidal modes predicted by the perturbation method, and they are apparently distinguishable from the numerical noise (see Fig. 2). Furthermore, the finite element solutions of the first (second) order modes follow very closely to the linear (quadratic) functions of $\delta^{\lambda}_{1,1}$ (solid lines in Fig. 2), as expected from the perturbation formulation.

By comparing Fig. 2 with fig. 2 in Qin *et al*. (2014) that shows the tidal responses due to $\delta\mu_0$, we find that the responses due to $\delta\lambda_0$ appear to be much weaker than the corresponding responses due to $\delta\mu_0$, for the same level of lateral variability. For the $\delta\lambda_0$ case, we also find that the (relative) gravitational response is about one order of magnitude weaker than the corresponding (relative) radial displacement response (Fig. 2). This is different from the $\delta\mu_0$ case where the (relative) gravitational and displacement responses are comparable [fig. 2 in Qin *et al*. (2014)]. For example, when $\delta^{\lambda}_{1,1} = 10$ per cent, the first order displacement responses, that is, $|h^{1'}_{3,1}(a)|$ from (2, 0) forcing and $|h^{1'}_{3,3}(a)|$ from (2, 2) forcing, are at the level of 10^{-3}, while the corresponding gravitational responses $|k^{1'}_{3,1}(a)|$ and $|k^{1'}_{3,3}(a)|$ are both at 10^{-4} level. In comparison, when $\delta^{\mu}_{1,1} = 10$ per cent, $|h^{1'}_{3,1}(a)|$ and $|k^{1'}_{3,1}(a)|$ from (2, 0) forcing and $|h^{1'}_{3,3}(a)|$ and $|k^{1'}_{3,3}(a)|$ from (2, 2) forcing are all greater than 10^{-2}. The mode $s^1(1, 1)$ is the only exception. The response $|h^{1'}_{1,1}(a)|$ to either (2, 0) or (2, 2) forcing is even larger than that from the $\delta\mu_0$ case, making $|h^{1'}_{1,1}(a)|$ comparable with the first order degree-3 responses (see Figs 2a and c; note that $|h^{1'}_{1,1}(a)|$ coincides with $|h^{1'}_{3,3}(a)|$ in Fig. 2c). Because the responses due to $\delta\lambda_0$ are relatively small, especially for the gravitational responses, they reach the numerical noise level of $\sim 10^{-6}$ (i.e. those dashed lines. Note that in Qin *et al*. (2014), we estimated this empirical noise level per our numerical resolution)

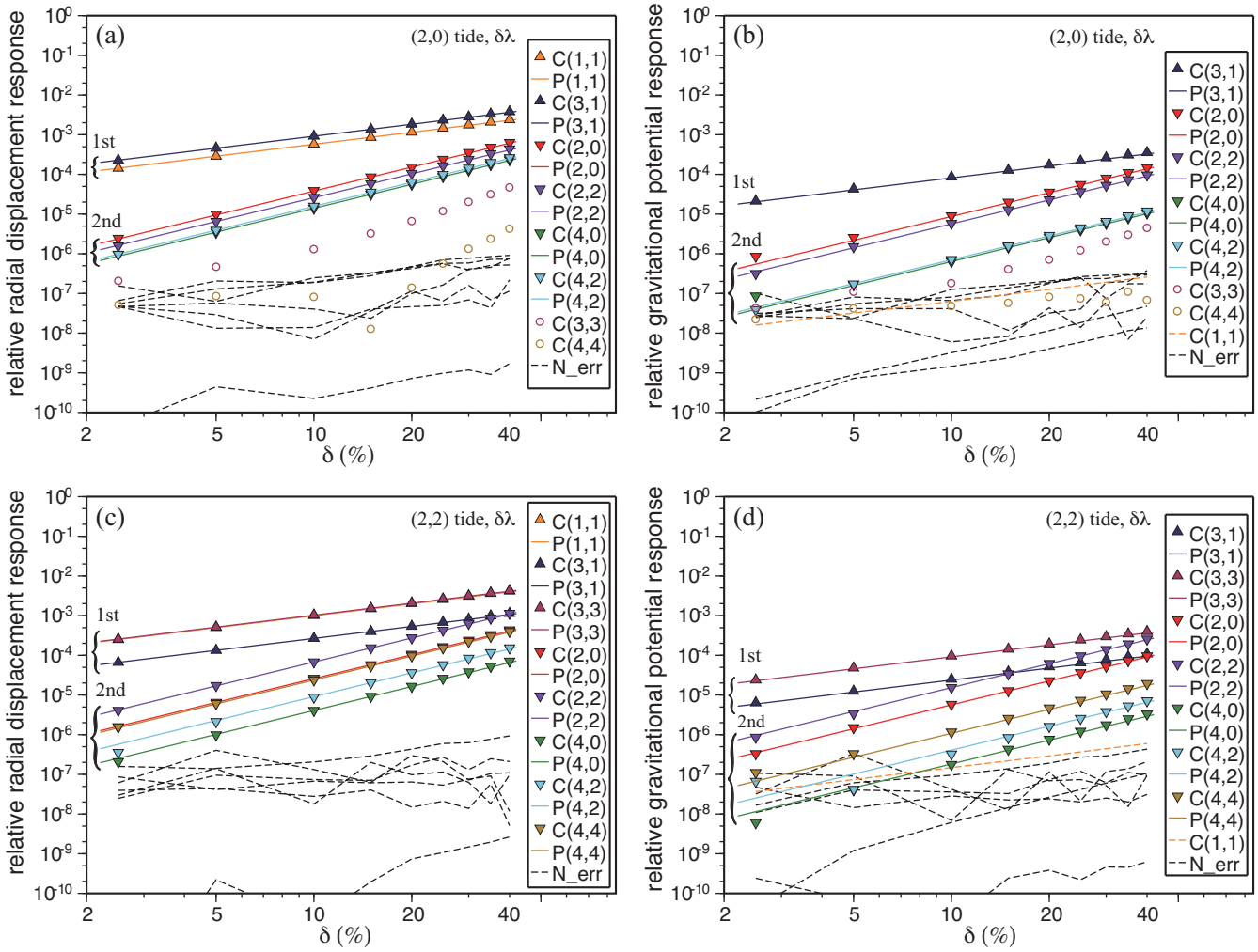

Figure 2. Relative responses (absolute values) in radial displacement (a,c) and gravitational potential (b,d) of the Moon with (1, 1) lateral heterogeneity in first Lamé parameter λ of the mantle, to (2, 0) (a,b) and (2, 2) (c,d) tidal forcing, from both the perturbation (solid lines) and finite element calculations (symbols and dashed lines). The plots are in a log–log scale. The lateral variability $\delta^{\lambda}_{1,1}$ is varied from 2.5 to 40 per cent. The solid straight lines represent all the first and second order response modes from the perturbation method (denoted by P). The triangles (first order), inverted triangles (second order) and open circles (higher than second order) represent the responses from the finite element results (denoted by C). The dashed lines represent all the other modes of harmonics $0 \le l \le 4$ and $0 \le m \le l$ from the finite element results, which are analysed to be the numerical artefacts.

when $\delta^{\lambda}_{1,1}$ is small. This explains why, for the $\delta\lambda_0$ case, the agreement on the gravitational responses between the two methods is relatively poor: some finite element solutions fluctuate around the perturbation solutions even by more than 10 per cent, like $s^2(4, 2)$ from (2, 2) forcing as one of the examples (Fig. 2 and Table 1).

We find that the significant differences between the tidal response solutions due to $\delta\lambda_0$ and $\delta\mu_0$ exist not only for (1, 1) lateral heterogeneity, but also exists for lateral heterogeneity of other harmonics. Thus, in general, when similar level of lateral heterogeneity exists in μ and λ, the tidal response due to $\delta\lambda_0$(especially for the gravitational potential) would be significantly smaller than that due to $\delta\mu_0$. Finally, like in Qin *et al*. (2014), the finite element solutions show some weak modes, such as $s(3, 3)$ and $s(4, 4)$ (marked by open circles in Figs 2a and b), and these modes are only expected from the third or higher order perturbation solutions according to the selection rule [eq. (22) in Qin *et al*. (2014)]. Although we cannot verify the accuracy for these modes using our second-order perturbation method, it is interesting to note that the responses at $s(3, 3)$ and $s(4, 4)$ are, respectively, approximately cubic and quartic functions of $\delta^{\lambda}_{1,1}$ for relatively large $\delta^{\lambda}_{1,1}$, as expected. Finite element solutions also display even weaker modes (i.e. the dotted and dashed lines in Fig. 2) that we consider as numerical errors, as they are not predicted from the perturbation solutions and do not show any systematic dependence on $\delta^{\lambda}_{1,1}$, similar to that in Qin *et al*. (2014).

All the benchmark results that have so far been presented are for radial displacement and gravitational potential responses, as in Fig. 2 and in Qin *et al*. (2014). No direct comparison has been made for horizontal displacement response, although fig. 3 of Qin *et al*. (2014) indirectly showed correct solutions for toroidal response in horizontal displacement. Here, we examine the tidal response solutions in horizontal displacement due to $\delta\mu_0$ and $\delta\lambda_0$ directly, as an additional validation of the perturbation method.

Table 1. Relative differences between perturbation and finite element solutions of modal responses to (2, 0) and (2, 2) tidal forces, respectively, due to (1, 1) lateral heterogeneity in shear modulus μ and first Lamé parameter λ of lateral variability $\delta^{\mu}_{1,1} = \delta^{\lambda}_{1,1} = 10$ per cent. k, h and l/w represent responses in gravitational potential, radial and horizontal displacements, respectively, as defined in eq. (73). Reference table 2 in Qin *et al*. (2014) for k and h results of $\delta\mu$ case.

	$\delta\lambda_0$			$\delta\mu_0$
Mode[a]	ε_k (%)[b]	ε_h (%)	$\varepsilon_l/\varepsilon_w$ (%)	$\varepsilon_l/\varepsilon_w$ (%)
$s^1(1, 1)_{(2,0)}$	–	0.62	0.21	0.12
$s^1(3, 1)_{(2,0)}$	5.07	0.48	0.04	1.42
$t^1(2, -1)_{(2,0)}$	–	–	–	0.41
$s^2(2, 0)_{(2,0)}$	3.31	2.37	1.44	0.52
$s^2(2, 2)_{(2,0)}$	0.82	0.37	0.87	0.97
$s^2(4, 0)_{(2,0)}$	1.84	0.19	0.36	0.46
$s^2(4, 2)_{(2,0)}$	1.61	0.07	0.57	2.88
$t^2(3, -2)_{(2,0)}$	–	–	–	0.63
$s^1(1, 1)_{(2,2)}$	–	0.66	0.04	0.31
$s^1(3, 1)_{(2,2)}$	6.86	0.93	0.42	0.91
$s^1(3, 3)_{(2,2)}$	5.34	0.50	0.14	0.73
$t^1(2, -1)_{(2,2)}$	–	–	–	0.44
$s^2(2, 0)_{(2,2)}$	1.29	0.38	1.00	0.69
$s^2(2, 2)_{(2,2)}$	0.95	0.49	0.91	0.53
$s^2(4, 0)_{(2,2)}$	1.96	0.18	1.14	0.23
$s^2(4, 2)_{(2,2)}$	21.2	1.95	1.49	0.63
$s^2(4, 4)_{(2,2)}$	8.36	0.33	0.26	1.65
$t^2(3, -2)_{(2,2)}$	–	–	–	0.69

[a]Spheroidal or toroidal mode of harmonic (l, m) induced by (2, 0) and (2, 2) tidal forcing, respectively.
[b]Percentage difference in the relative response X, $\varepsilon_X = |(X_{\text{Citcom}} - X_{\text{pert}})/X_{\text{pert}}|$, where X can be k (potential), h (radial displacement), l and w (horizontal displacement of spheroidal and toroidal, respectively).

We add a post-processing functionality into our finite element code to perform VSH expansion on the surface horizontal displacement field $\boldsymbol{u}_{\text{h}}$, such that

$$\boldsymbol{u}_{\text{h}} = \boldsymbol{u}_{\text{h}}(a, \theta, \phi) = \sum_{l,m} V^D_{lm}(a)\boldsymbol{B}_{lm} + W^D_{lm}(a)\boldsymbol{C}_{lm}, \tag{74}$$

which contains both spheroidal and toroidal components of horizontal displacement. Per the selection rule for degree-2 tidal force and (1, 1) lateral heterogeneity, we only need to examine certain spheroidal and toroidal modes in our benchmarks, that is, $1 \le l \le 4$ and $0 \le m \le l$ ($-l \le m < 0$) for spheroidal (toroidal) modes. Using the expansion coefficients of the finite element solutions from eq. (74), we compute the relative horizontal displacement responses $|l^{D'}_{lm}(a)|$ and $|w^{D'}_{lm}(a)|$ for spheroidal and toroidal modes [see eq. (73)], respectively, and plot them together against the perturbation solutions.

Results are shown in Fig. 3 for four individual cases: (2, 0) and (2, 2) forcing on $\delta\mu_0$ (top panels) and $\delta\lambda_0$ (bottom panels), respectively. Again, all the first and the second order spheroidal and toroidal modes (triangles and squares in Fig. 3, respectively) predicted by the perturbation method are also the most significant modes from the finite element solutions, and the perturbation solutions (solid lines in Fig. 3) match the corresponding finite element solutions remarkably well (Fig. 3 and Table 1). Also, the horizontal displacement responses due to $\delta\mu_0$ are larger than those due to $\delta\lambda_0$ by on average an order of magnitude (Figs 3a and b verse c and d), similar to what we find for radial displacement responses. The (relative) horizontal displacement responses (Fig. 3) are similar in amplitude to the radial displacement responses (Fig. 2 for $\delta\lambda_0$ and fig. 2 of Qin *et al*. (2014) for $\delta\mu_0$). An exception is mode $s^1(1, 1)$ due to $\delta\mu_0$. The horizontal displacement response $|l^{1'}_{1,1}(a)|$ is one of the largest responses and is about two orders of magnitude larger than the corresponding radial displacement response $|h^{1'}_{1,1}(a)|$ [Figs 3a and b verse fig. 2 of Qin *et al*. (2014)].

For $\delta\mu_0$ cases, both (2, 0) and (2, 2) forces induce the same set of toroidal modes in the response, which are $t^1(2, -1)$ and $t^2(3, -2)$. The toroidal response $|w^{1'}_{2,-1}(a)|$ is surprisingly large, especially for that induced by (2, 0) forcing, and when $\delta^{\mu}_{1,1}$ is sufficiently large (e.g. $\delta^{\mu}_{1,1} \ge 30$ per cent), $|w^{1'}_{2,-1}(a)|$ is even close to 1. The finite element solutions clearly show toroidal modes $t^3(4, -1)$ and $t^3(4, -3)$ (open diamonds in Figs 3a and b). Although these two modes are predicted to exist at the third order of perturbation, their responses are at the same level as those second order degree-4 responses. Note that $\delta\lambda_0$ does not induce any toroidal modes, which is evident in Figs 3(c) and (d): $|w^{1'}_{2,-1}(a)|$ and $|w^{2'}_{3,-2}(a)|$ are both at the noise level (dashed lines in corresponding colours).

4.2 Density anomaly effect on tidal response

We now explore the effect of lateral heterogeneity in density ρ on tidal response. Because including density anomaly $\delta\rho_0$ brings additional force balance terms into the governing equations, it is unclear how this complication can be implemented in our current finite element formulation.

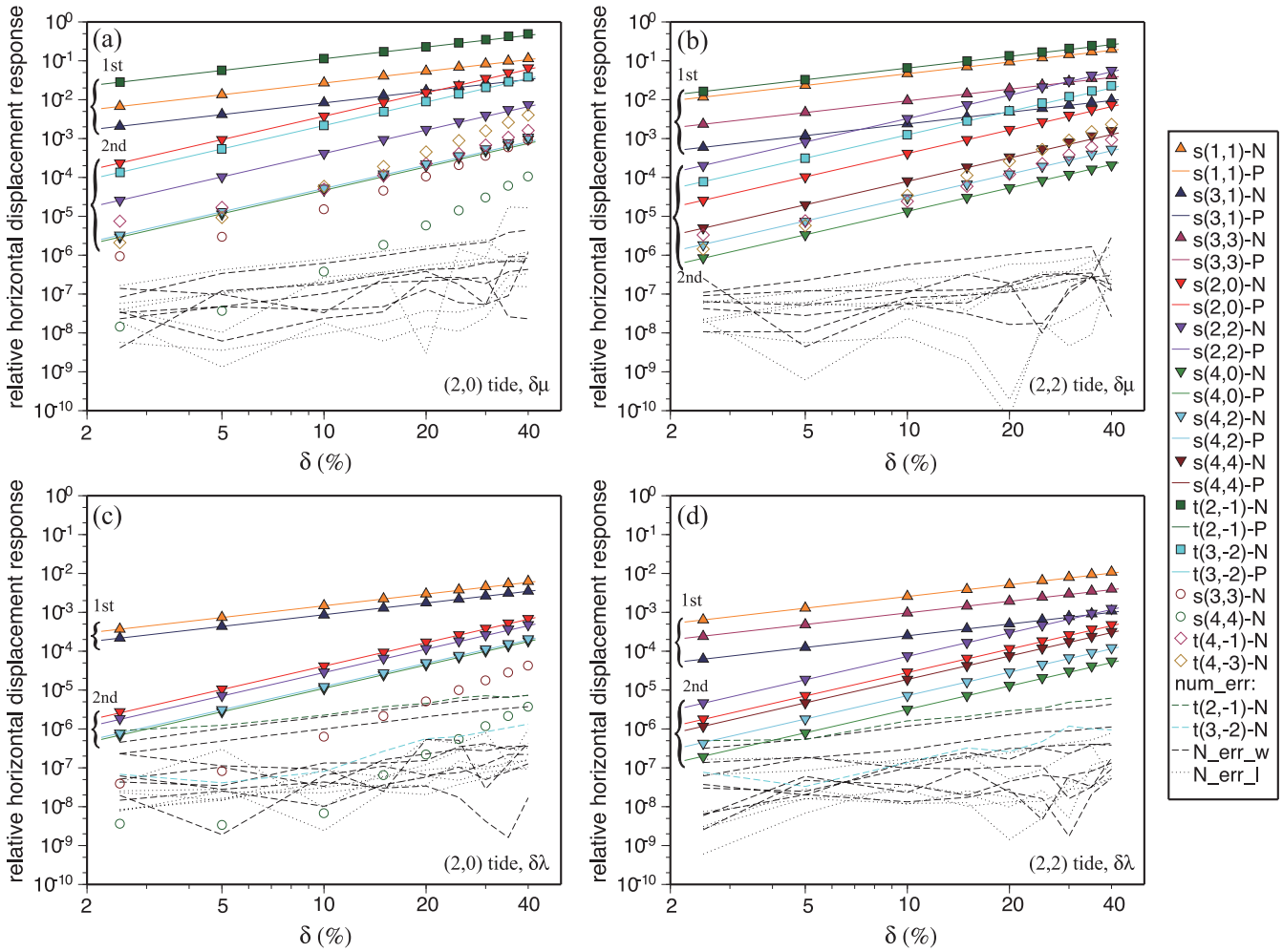

Figure 3. Relative responses (absolute values) in horizontal displacement of the Moon with (1, 1) lateral heterogeneity in shear modulus μ (a,b) and first Lamé parameter λ (c,d) of the mantle, respectively, to (2, 0) (a,c) and (2, 2) (b,d) tidal forcing, from both the perturbation (solid lines) and finite element calculations (symbols and dashed and dotted lines). The plots are in a log–log scale. The lateral variabilities $\delta^{\mu}_{1,1}$ and $\delta^{\lambda}_{1,1}$ are varied from 2.5 to 40 per cent. The solid straight lines represent the first and second order response modes from the perturbation method (denoted by P). The triangles (first order), inverted triangles (second order) and open circles (higher than second order) represent the real spheroidal responses from the finite element results (denoted by N). The squares (first and second order) and open diamonds (higher than second order) represent the real toroidal responses from the finite element results (denoted by N). The dotted and dashed lines represent all the other spheroidal and toroidal modes of harmonics $0 \leq l \leq 4$ from the finite element results, respectively, and are numerical artefacts.

Therefore, similar benchmark calculations done for $\delta\mu_0$ and $\delta\lambda_0$ cannot be done for $\delta\rho_0$ case. Instead, we only show the perturbation solutions for $\delta\rho_0$ and compare them with those for $\delta\mu_0$. In this study, we only consider a (1, 1) lateral heterogeneity in density.

We first determine a reasonable lateral variability for a 3-D density structure. In the Earth, the largest heterogeneities are present in the uppermost (top 200 km, including the crust) and the lowermost (bottom 300 km) mantle. Acknowledging that the shear velocity variation ($\delta v_s/v_s$) can reach ~10 per cent in the Earth's uppermost mantle (e.g. Shapiro & Ritzwoller 2002) and ~2.5 per cent at long wavelengths in the deep mantle (e.g. Su & Dziewonski 1997), a 10 per cent lateral variability is approximately a global upper bound for lateral heterogeneities in the elastic structures (note that the shear modulus variation is approximately twice as much as the shear velocity variation), which may also be true for the Moon. In comparison, the density variation ($\delta\rho/\rho$) in the Earth's mantle is on average less than 2 per cent (e.g. Hager & Richards 1989). For the lunar mantle, we estimate the density variation from thermal or thermochemical convection models. For example, in Zhong *et al.* (2000), the onset of degree-1 thermochemical convection ~4 Ga introduces less than 1 per cent density variation in different models. In Laneuville *et al.* (2013), long-term thermal convections can cause on average a less than 2 per cent density variation in the present-day lunar mantle. Here we choose $\delta^{\rho}_{1,1} = 2.5$ per cent for $\delta\rho_0$ in our calculation, and compare the tidal response with that due to $\delta\mu_0$ at a $\delta^{\mu}_{1,1} = 10$ per cent level.

$\delta\rho_0$ and $\delta\mu_0$ induce the same set of high order modes (Fig. 1). We calculate the relative response (i.e. $k^{D'}_{lm}$, $h^{D'}_{lm}$, $l^{D'}_{lm}$ and $w^{D'}_{lm}$) of every mode from $\delta\rho_0$ and $\delta\mu_0$ to (2, 0) and (2, 2) forcing, respectively. Fig. 4 shows the absolute values of the response for each mode from $\delta\rho_0$ and $\delta\mu_0$ case, represented by coloured bars (response without a bar is smaller than 10^{-5}). The diamond on the bar indicates that response has a negative value. We find that most first order responses due to $\delta\rho_0$ and $\delta\mu_0$ (except for $h^{1'}_{1,1}$) are comparable in amplitude, while the second order responses due to $\delta\rho_0$ are all smaller than those due to $\delta\mu_0$ and the degree-4 spheroidal and degree-3 toroidal responses are orders of magnitude weaker. More interestingly, all the first order modes due to $\delta\rho_0$ and $\delta\mu_0$ have opposite signs in response. Because the first order

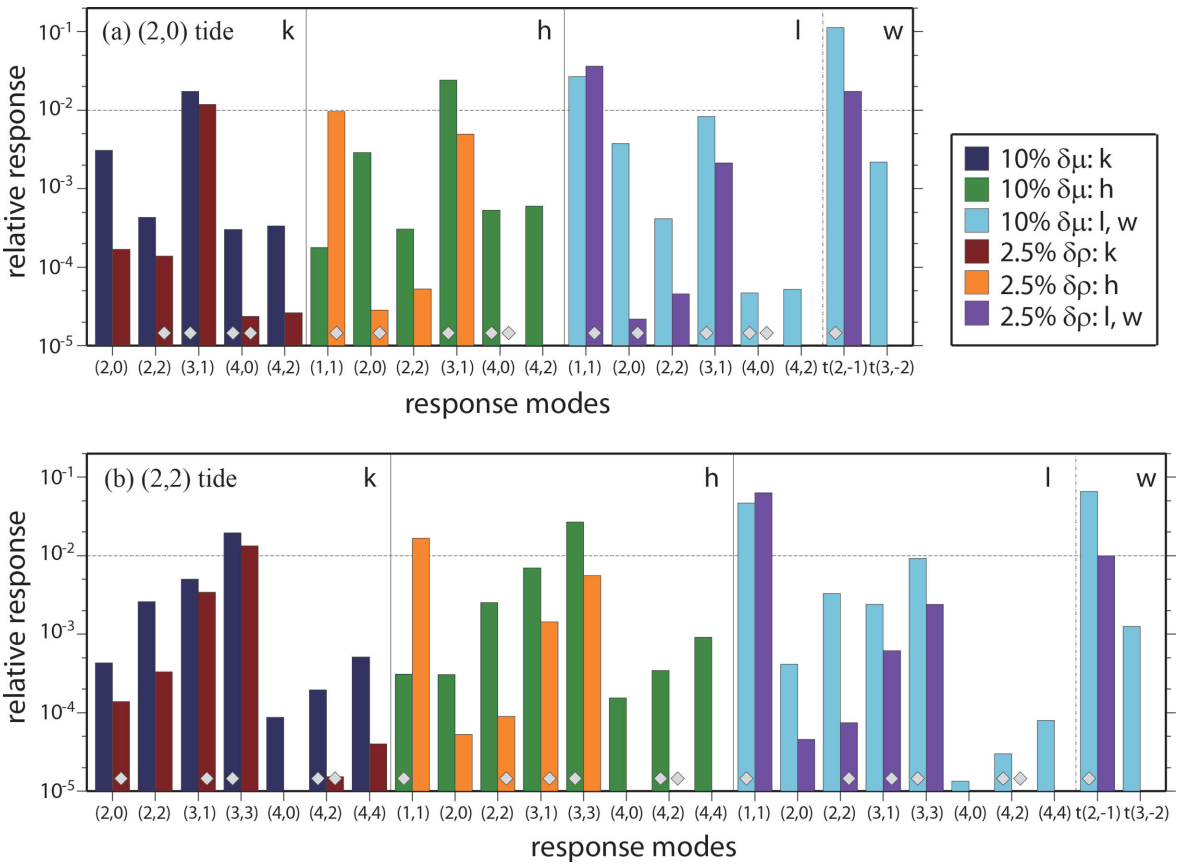

Figure 4. Comparisons of high order tidal responses of the Moon induced respectively by (1, 1) lateral heterogeneities in shear modulus μ ($\delta^{\mu}_{1,1} = 10$ per cent) and density ρ ($\delta^{\rho}_{1,1} = 2.5$ per cent) of the mantle. Panels (a) and (b) show the responses in gravitational potential (k), radial displacement (h) and horizontal displacement (l and w) to (2, 0) and (2, 2) tidal forcing, respectively, for the modes that are marked on the horizontal axis (modes without an initial letter are spheroidal). The absolute values of the relative responses are measured by the heights of the coloured bars in log scale. Responses that are smaller than 10^{-5} are not shown. The grey diamond on a bar indicates that this response is negative.

response is proportional to δ, its sign is controlled by the choice of δ. In Qin *et al*. (2012), we proposed a (1, 1) laterally heterogeneous structure in the lunar mantle that depicts a hotter but chemically denser region at depth, which implies a reduced shear modulus (i.e. $\delta^{\mu}_{1,1} > 0$) and a positive density anomaly (i.e. $\delta^{\rho}_{1,1} < 0$) within that region. As a result, the first order responses induced by $\delta\rho_0$ and $\delta\mu_0$ would add to each other, enhancing the total responses. On the other hand, if lateral variations in density and shear modulus are both caused by thermal effects (i.e. for hot regions, $\delta^{\rho}_{1,1} > 0$ and $\delta^{\mu}_{1,1} > 0$), their combined effects may reduce those responses. In Zhong *et al*. (2012), we asserted that $\delta\mu_0$ could induce degree-3 tidal response in the Moon's gravitational potential, which could be a promising measurable quantity to constrain the (1, 1) structure in the lunar mantle. Now, the combined effects of $\delta\rho_0$ and $\delta\mu_0$ may make detection of the degree-3 spheroidal responses, if there were, more plausible.

4.3 Tidal effect of lunar crustal thickness variations

The crustal thickness of the Moon has been well studied from recent geodetic measurements and significant thickness variations are found to exist (e.g. Wieczorek *et al*. 2013). For example, many nearside impact basins are depleted with crustal materials, while the crust beneath the farside highlands is as thick as over 50 km (e.g. Wieczorek *et al*. 2013). Here we use the perturbation method to evaluate the effect of lunar crust thickness variation on the tidal response, with the goal to answer one question concerning future measurements: would the lunar crust (top tens of kilometres) have a significant impact on the tidal response, compared to a laterally heterogeneous structure in the deep mantle?

We calculate the gravitational tidal response caused by the lunar crust. Because a non-spherical material interface such as the undulated crust–mantle boundary or Moho cannot be directly formulated into our perturbation method, crustal thickness variations are modelled as lateral heterogeneities in the material properties in our calculations. We adopt a crustal thickness model from Wieczorek *et al*. (2013; Fig. 5a), but we find that our results are insensitive to different crustal thickness models. This crustal model has a mean crustal thickness of 34 km. We call the top layer with the mean crustal thickness of 34 km as layer L1 and the layer below L1 and above the deepest point of Moho as L2 (Fig. 5b). Material properties below L2 are considered purely 1-D. We may reasonably assume a full compensation in the lunar crust and uppermost mantle at long wavelengths, and thus ignore any density anomaly effect on the tidal response. We use a simple strategy to map the

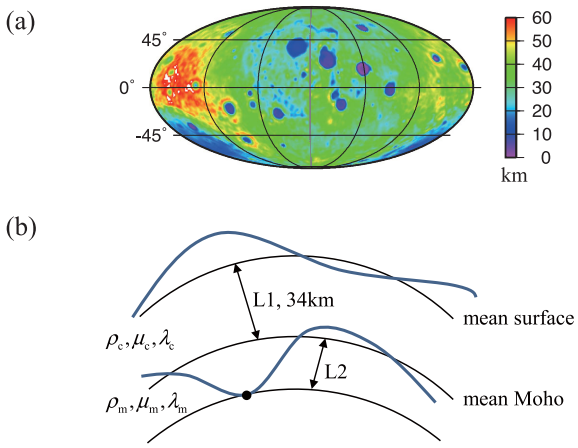

Figure 5. (a) Map of lunar crustal thickness variations (Wieczorek *et al*. 2013) in Mollweide projection centred on the sub-Earth point. The mean thickness of the crust is 34 km. (b) Schematic of converting surface and Moho topographies into lateral heterogeneities in shear modulus μ and first Lamé parameter λ in the mean crustal layer L1 and the topmost mantle layer L2 (L1 and L2 are defined in Section 4.3 of the main context).

crustal thickness onto lateral variations in shear modulus μ and Lamé parameter λ in layers L1 and L2, as illustrated in Fig. 5(b), using the following linear conversions (the same mapping is used for μ and λ but is shown only for μ here)

$$\text{L1}: \quad \mu^1(\theta,\phi) = \begin{cases} [(h_s - h_m + D_1)\mu_c + h_m\mu_m]/D_1 & \text{if } h_m > 0 \\ (h_s + D_1)\mu_c/D_1 & \text{if } h_m < 0 \end{cases},$$
$$\text{L2}: \quad \mu^2(\theta,\phi) = \begin{cases} \mu_m & \text{if } h_m > 0 \\ [(-h_m)\mu_c + (h_m + D_2)\mu_m]/D_2 & \text{if } h_m < 0 \end{cases} \tag{75}$$

where $h_s = h_s(\theta,\phi)$ and $h_m = h_m(\theta,\phi)$ are the surface and Moho topographies, respectively, D_1 and D_2 are thickness of layers L1 and L2, respectively, μ_c and μ_m are shear modulus of the crust and the uppermost mantle, respectively, and usually $\mu_m > \mu_s$.

Fig. 6(a) shows the maps of percentage differences in μ (top panels) and λ (bottom panels) from reference values in layers L1 (left) and L2 (right), respectively. The thinner crust on the nearside leads to larger values of elastic moduli in L1, since mantle material intrudes into L1 (Fig. 6a). The thicker farside crust results in larger elastic moduli in L1 and smaller elastic moduli in L2 (Fig. 6a). In order for the modelled laterally varying elastic structures to be included in our calculations, they are expanded into SHs of degrees and orders up to 5. This is because degree 5 is the highest SH degree of an eigenstructure to induce a degree-3 first-order response, when coupled with degree-2 tidal force. Fig. 6(b) shows lateral variabilities of μ and λ in layers L1 and L2, respectively, for harmonics of degrees 1 to 5. It is obvious that layers L1 and L2 are dominated by (2, 1) and (1, 1) structures, respectively. Also, lateral variabilities in μ and λ are very similar. Since lateral heterogeneity in λ has a much weaker effect on tidal response than that from μ, as discussed in Section 4.1, we ignore the effect of lateral heterogeneity in λ in our calculations.

The gravitational tidal response is calculated using the shear modulus structures in layers L1 and L2 (Fig. 6b), and is shown up to degree 4 by the dark grey bars in Fig. 7, for (2, 0) and (2, 2) tidal forcing, separately. We find that the crust-induced tidal response is only at a 10^{-4} level and is dominated at some degree-2 and degree-3 modes. To compare with a deep structure, we calculate the tidal response caused by a (1, 1) structure in shear modulus in the deep interior of the mantle for three cases: 1) 5 per cent lateral variability in the bottom half (~700 km in thickness) of the mantle (red squares in Fig. 7), 2) 2.5 per cent lateral variability in the bottom half of the mantle (navy squares) and 3) 5 per cent lateral variability in the bottom quarter (~350 km in thickness) of the mantle (green squares). We observe that all the second order responses caused by the (1, 1) deep mantle structure are small (i.e. those degree-2 and 4 responses) and are overwhelmed by the responses caused by the crust (Fig. 7). However, since the first order responses (i.e. the degree-3 responses) are significantly stronger than the second order ones, the degree-3 responses far exceed the crustal effect, for all three cases (Fig. 7). It thus suggests that the tidal effect from the lunar crustal thickness variation is not significant, and it would not degrade the promise of using degree-3 tidal response measurements to constrain the degree-1 lunar mantle structure (Zhong *et al*. 2012), even if such potential structure is relatively deep and weak.

We also examine the sensitivity of tidal response to depth location of the (1, 1) mantle structure. We do this by calculating the sensitivity kernels as function of radius for the first order degree-3 responses. We divide the lunar mantle equally into 60 layers (23.5 km thick for each layer) and perturb the shear modulus in each layer with a (1, 1) structure of 10 per cent lateral variability. We then calculate the first order degree-3 gravitational responses to (2, 0) and (2, 2) forcing, for lateral heterogeneity in each of the 60 layers. All the response solutions at different depths are normalized by the maximum solution value, and are plotted against the radius of the middle of each layer, that is, the sensitivity kernels, in Fig. 8. We find that none of the degree-3 gravitational responses would change signs with radius, suggesting that the responses due to lateral heterogeneities at different depths would add to each other without cancellation effect, as long as the heterogeneities

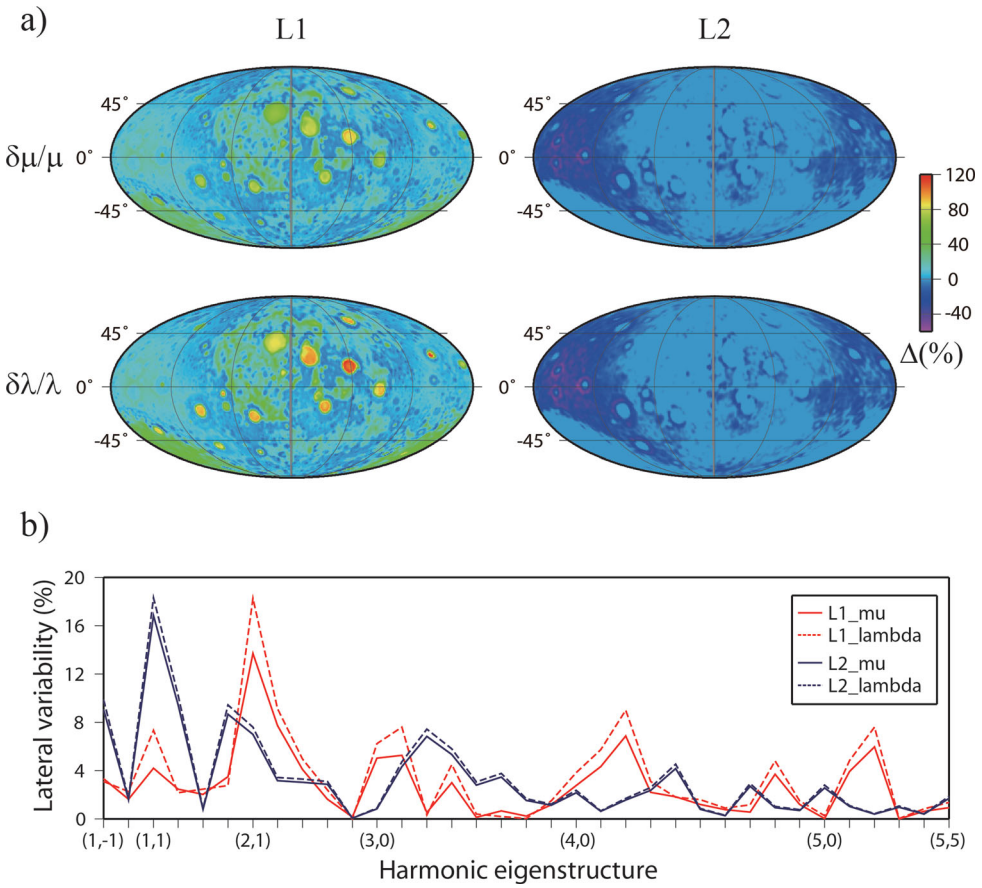

Figure 6. Laterally varying (3-D) elastic structures in the two topmost layers (L1 and L2) of the Moon from conversion of the lunar crustal thickness variations. (a) Maps of lateral variabilities in percentage in shear modulus μ (top panels) and first Lamé parameter λ (bottom panels) in layers L1 and L2, respectively. The maps are in Mollweide projection and are centred on the sub-Earth point. (b) Lateral variabilities in μ (solid lines) and λ (dashed lines) in layers L1 (red) and L2 (navy) for harmonic eigenstructures up to (5, 5). Eigenstructures are marked on horizontal axis in an ascending order of harmonic degree and order, from (1, −1) to (5, 5).

have the same positive or negative signs. Fig. 8 also shows that the degree-3 gravitational tidal response is more sensitive to the (1, 1) structure at intermediate depths than that near the surface or the CMB. We find that this is also true for first order gravitational tidal responses due to non-degree-1 mantle structures. This suggests that a laterally heterogeneous structure is more likely to be detected from geodetic (gravity) measurements if it exists in the mid-mantle of the Moon, compared to that near the surface or the CMB.

5 CONCLUSION AND DISCUSSION

We have developed a complete perturbation method for calculating the elastic response of a laterally heterogeneous (3-D) planetary body to time-varying body tidal forcing, by incorporating both 3-D elastic and density structures of the mantle into one formulation. As done in our previous study (Qin *et al*. 2014), we apply the perturbation method to a laterally varying Moon with an SH degree 1 and order 1 (i.e. (1, 1)) heterogeneity in its elastic or density structure, and solve its response to degree-2 tidal forcing at the accuracy of second order in perturbation. We verify the perturbation method by comparing the perturbation solutions with those from a finite element method, for responses not only in gravitational potential and radial displacement but also, for the first time, in horizontal displacement. The excellent agreement between the results from these two methods indicates that the formulation and implementation of the perturbation method is correct.

In deriving the perturbation equations, lateral heterogeneity in density (i.e. density anomaly) is treated differently from those in elastic moduli, due to involvement of a more complex physical process. First, density anomaly acts as buoyancy that drives the mantle flow, causing a pre-stressed and deformed background state before tidal force is being applied. In order to obtain a linearized perturbation formulation, we ignore the pre-stress effect, as done commonly in similar analyses. Second, tidal force acting on a 3-D density structure may potentially cause a net force on the system, which would cause force imbalance in the equation of motion and spurious solutions for tidal deformation. To resolve this problem, we introduce an inertial force into the system that zeroes out the effect of the net force.

The perturbation method allows investigations of the impact of individual sources of lateral heterogeneity on tidal response as well as their combined effect. By comparing the individual effects of a (1, 1) lateral heterogeneity in two elastic moduli and density on the lunar tidal response (e.g. using lateral variability upper bounds of 10 and 2.5 per cent for elastic moduli and density, respectively), we find that (1)

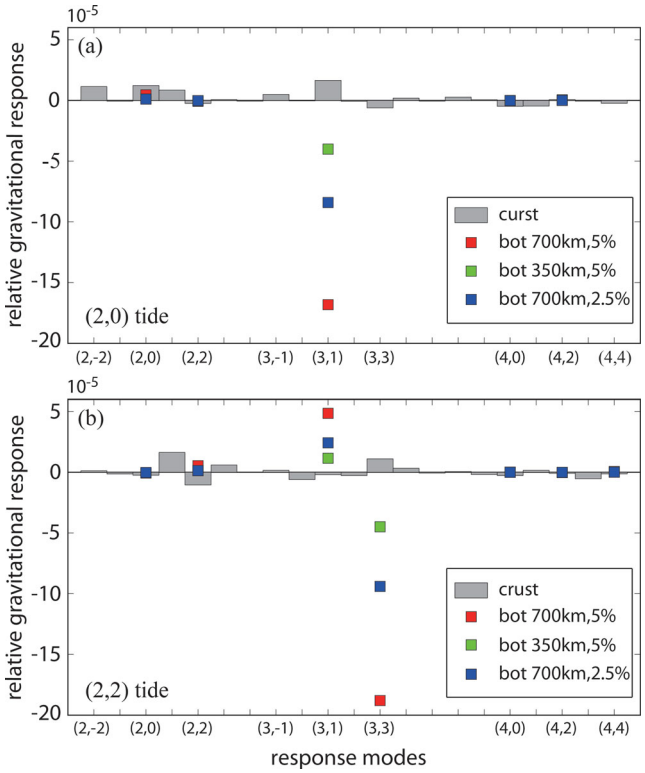

Figure 7. High order gravitational responses of the Moon to (2, 0) (a) and (2, 2) (b) tidal forcing, due to the lunar crustal thickness variations (grey bars) and a (1, 1) elastic structure in the deep mantle (coloured squares), respectively, computed by the perturbation method. The horizontal axis marks the response modes from harmonic (2, −2) to (4, 4) in an ascending order of harmonic degree and order. Red, navy and green squares represent the tidal responses for three different depths and amplitudes of the (1, 1) structure in shear modulus μ, as described in the inset.

lateral heterogeneity in shear modulus has the greatest impact on the tidal response, (2) lateral heterogeneities in density and shear modulus have comparable first order tidal effects, (3) the effect of lateral heterogeneity in first Lamé parameter is 1 to 2 orders of magnitude weaker than that of shear modulus or density. These findings apply also to lateral heterogeneity at other wavelengths. Therefore, in general, lateral heterogeneities in shear modulus and density are primary contributions to high order tidal responses.

Exploring the possibility in using degree-3 tidal responses to constrain degree-1 (i.e. the longest wavelength) lunar mantle structure is one of the main motivations of our study. In Zhong *et al*. (2012) and Qin *et al*. (2014), we found that a (1, 1) lateral heterogeneity in shear modulus varying at 10 per cent level throughout the lunar mantle could cause $>$ 2 per cent degree-3 (relative) tidal responses, which is significant. Now by including lateral heterogeneity in density, we find that reduced (enhanced) shear modulus accompanied by positive (negative) density anomaly in one hemisphere of the Moon would always reinforce the degree-3 responses, which is true not only for (1, 1) structure but also for other degree-1 structures [i.e. (1, 0) or (1, −1)]. Thus, if the mantle on the nearside of the Moon has both higher temperature and larger density, as proposed for a thermochemical mantle structure in Qin *et al*. (2012), the degree-3 tidal responses would be significantly stronger than those with the shear modulus effect only. In contrary, if mantle convection in the Moon is purely thermally driven, as proposed by Laneuville *et al*. (2013), the degree-1 component of hotter and less dense upwelling (i.e. smaller shear modulus and density than the ambient mantle) would reduce the degree-3 responses, making detection of the mantle structure more difficult.

Moreover, we evaluate the impact of lunar crust thickness variations on the tidal response, as a more realistic application of the perturbation method. The crustal thickness variations are modelled as lateral heterogeneities in the elastic properties in the crust and the mantle such that they can be included in the perturbation formulation. The calculations show that the crustal thickness variations of the Moon, although significant, would have a much smaller effect on the degree-3 tidal responses, compared to a much weaker degree-1 elastic structure in the mantle. This suggests that the degree-3 tidal responses can indeed help constrain the degree-1 lunar mantle structure.

Determination of degree-3 tidal Love numbers of different harmonic orders would help significantly constrain the degree-1 mantle structure of the Moon. Knowledge of higher degree Love numbers, if possible, can put better constraints on the interior structure of a planet. For example, degree-4 Love numbers can be used to constrain degree-2 structures as well as add tighter constraint to degree-1 structures. However, we recognize the challenges in extracting these Love numbers from existing geodetic observations. While the GRAIL mission has made good progress in improving degree-2 Love numbers (e.g. Konopliv *et al*. 2013; Lemoine *et al*. 2013; Williams *et al*. 2014), it remains unclear whether the GRAIL data can yield higher order Love numbers. However, regardless of the outcome with the GRAIL mission on higher order Love numbers, we think that our perturbation method for computing tidal deformation for 3-D planetary bodies may have applications to future targeted missions to the Moon, Mercury or icy satellites.

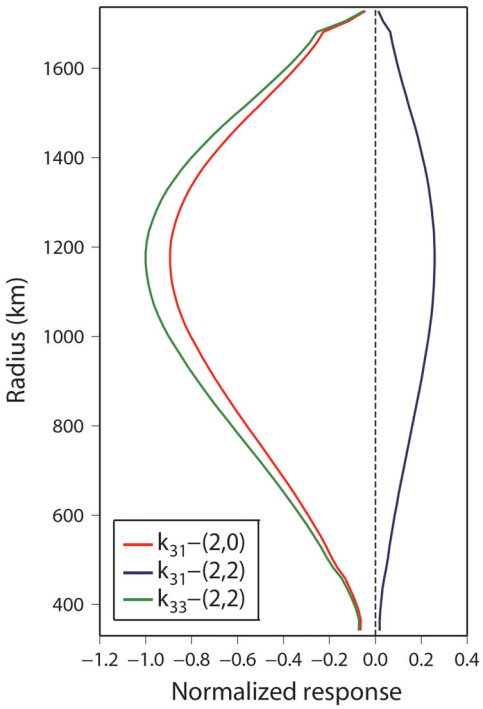

Figure 8. Sensitivity kernels (normalized) of the first order degree-3 gravitational responses to (2, 0) and (2, 2) tidal forcing for (1, 1) lateral heterogeneity in shear modulus μ, as functions of the radius. The red, navy and green curves represent kernels of (3, 1) response to (2, 0) forcing, (3, 1) response to (2, 2) forcing and (3, 3) response to (2, 2) forcing, respectively.

ACKNOWLEDGEMENTS

This work is supported by a grant from NASA (NNX14AQ06G). We thank Dr Nicola Tosi and Dr Konstantin Latychev for their valuable comments and suggestions to our work.

REFERENCES

A, G., Wahr, J. & Zhong, S., 2013. Computations of the viscoelastic response of a 3-D compressible Earth to surface loading: an application to Glacial Isostatic Adjustment in Antarctica and Canada, *Geophys. J. Int.*, **192**, 557–572.

Anderson, B.J. *et al.*, 2011. The global magnetic field of Mercury from MESSENGER orbital observations, *Science*, **333**, 1859–1862.

Dahlen, F.A. & Tromp, J., 1998. *Theoretical Global Seismology*, pp. 268–271, Princeton Univ. Press.

Farrell, W.E., 1972. Deformation of the Earth by surface loads, *Rev. Geophys.*, **10**, 761–797.

Hager, B.H. & Richards, M.A., 1989. Long-wavelength variations in Earth's geoid: physical models and dynamical implications, *Phil. Trans. R. Soc. Lond., A*, **328**, 309–327.

Konopliv, A.S. *et al.*, 2013. The JPL lunar gravity field to spherical harmonic degree 660 from the GRAIL primary mission, *J. geophys. Res.*, **118**, 1415–1434.

Laneuville, M., Wieczorek, M.A., Breuer, D. & Tosi, N., 2013. Asymmetric thermal evolution of the Moon, *J. geophys. Res.*, **118**(7), 1435–1452.

Latychev, K., Mitrovica, J.X., Ishii, M., Chan, N.-H. & Davis, J.L., 2009. Body tides on a 3-D elastic earth: toward a tidal tomography, *Earth planet. Sci. Lett.*, **277**, 86–90.

Lau, H.C., Yang, H.-Y., Tromp, J., Mitrovica, J.X., Latychev, K. & Al-Attar, D., 2015. A normal mode treatment of semi-diurnal body tides on an aspherical, rotating and anelastic Earth, *Geophys. J. Int.*, **202**(2), 1392–1406.

Lawrence, D.J., Feldman, W.C., Barraclough, B.L., Binder, A.B., Elphic, R.C., Maurice, S. & Thomsen, D.R., 1998. Global elemental maps of the Moon: the Lunar Prospector gamma-ray spectrometer, *Science*, **281**, 1484–1489.

Lawrence, D.J., Feldman, W.C., Elphic, R.C., Little, R.C., Prettyman, T.H., Maurice, S., Lucey, P.G. & Binder, A.B., 2002. Iron abundances on the lunar surface as measured by the Lunar Prospector gamma-ray and neutron spectrometers, *J. geophys. Res.*, **107**(E12), 13-1–13-26.

Lemoine, F.G. *et al.*, 2013. High-degree gravity models from GRAIL primary mission data, *J. geophys. Res.*, **118**, 1676–1698.

Longman, I.M., 1962. A Green's function for determining the deformation of the Earth under surface mass loads: 1. Theory, *J. geophys. Res.*, **67**, 845–850.

Longman, I.M., 1963. A Green's function for determining the deformation of the Earth under surface mass loads: 2. Computations and numerical results, *J. geophys. Res.*, **68**, 485–496.

Love, A.E.H., 1911. *Some Problems of Geodynamics*, Cambridge Univ. Press.

Nakamura, Y., 2005. Farside deep moonquakes and deep interior of the Moon, *J. geophys. Res.*, **110**, E01001, doi:10.1029/2004JE002332.

Porco, C.C. *et al.*, 2006. Cassini observes the active south pole of Enceladus, *Science*, **311**, 1393–1401.

Qin, C., Muirhead, A.C. & Zhong, S., 2012. Correlation of deep moonquakes and mare basalts: implications for lunar mantle structure and evolution, *Icarus*, **220**, 100–105.

Qin, C., Zhong, S. & Wahr, J., 2014. A perturbation method and its application: elastic tidal response of a laterally heterogeneous planet, *Geophys. J. Int.*, **199**(2), 631–647.

Shapiro, N.M. & Ritzwoller, M.H., 2002. Monte-Carlo inversion for a global shear-velocity model of the crust and upper mantle, *Geophys. J. Int.*, **151**(1), 88–105.

Smith, D.E., Zuber, M.T., Neumann, G.A. & Lemoine, F.G., 1997. Topography of the Moon from the Clementine lidar, *J. geophys. Res.*, **102**(E1), 1591–1611.

Smith, D.E. *et al.*, 2010. The lunar orbiter laser altimeter investigation on the lunar reconnaissance orbiter mission, *Space Sci. Rev.*, **150**, 209–241.
Spencer, J.R. *et al.*, 2006. Cassini encounters Enceladus: background and the discovery of a south polar hot spot, *Science*, **311**, 1401–1405.
Su, W. & Dziewonski, A.M., 1997. Simultaneous inversion for 3-D variations in shear and bulk velocity in the mantle, *Phys. Earth planet. Inter.*, **100**, 135–156.
Tapley, B.D., Bettadpur, S., Watkins, M. & Reigber, C., 2004. The gravity recovery and climate experiment: mission overview and early results, *Geophys. Res. Lett.*, **31**(9), doi:10.1029/2004GL019920.
Tompkins, S. & Pieters, C.M., 1999. Mineralogy of the lunar crust: results from Clementine, *Meteorit. Planet. Sci.*, **34**, 25–41.
Tromp, J. & Mitrovica, J.X., 1999a. Surface loading of a viscoelastic earth–I. General theory, *Geophys. J. Int.*, **137**, 847–855.
Tromp, J. & Mitrovica, J.X., 1999b. Surface loading of a viscoelastic earth–II. Spherical models, *Geophys. J. Int.*, **137**, 856–872.
Wahr, J., Selvans, Z.A., Mullen, M.E., Barr, A.C., Collins, G.C., Selvans, M.M. & Pappalardo, R.T., 2009. Modeling stresses on satellites due to nonsynchronous rotation and orbital eccentricity using gravitational potential theory, *Icarus*, **200**, 188–206.
Weber, R.C., Lin, P.Y., Garnero, E.J., Williams, Q. & Lognonne, P., 2011. Seismic detection of the lunar core, *Science*, **331**, 309–312.
Wieczorek, M.A. *et al.*, 2006. The constitution and structure of the lunar interior, *Rev. Mineral. Geochem.*, **60**, 221–364.
Wieczorek, M.A. *et al.*, 2013. The crust of the Moon as seen by GRAIL, *Science*, **339**, 671–675.
Williams, J.G. *et al.*, 2014. Lunar interior properties from the GRAIL mission, *J. geophys. Res.*, **119**, 1546–1578.
Zhong, S., Parmentier, E.M. & Zuber, M.T., 2000. A dynamic origin for the global asymmetry of lunar mare basalts, *Earth planet. Sci. Lett.*, **177**(3), 131–140.
Zhong, S., Paulson, A. & Wahr, J., 2003. Three-dimensional finite-element modelling of Earth's viscoelastic deformation: effects of lateral variations in lithospheric thickness, *Geophys. J. Int.*, **155**, 679–695.
Zhong, S., Qin, C., A, G. & Wahr, J., 2012. Can tidal tomography be used to unravel the long-wavelength structure of the lunar interior?, *Geophys. Res. Lett.*, **39**, L15201, doi:10.1029/2012GL052362.
Zuber, M.T., 2001. The crust and mantle of Mars, *Nature*, **412**, 220–227.
Zuber, M.T., Smith, D.E., Lemoine, F.G. & Neumann, G.A., 1994. The shape and internal structure of the Moon from the Clementine mission, *Science*, **266**, 1839–1843.
Zuber, M.T. *et al.*, 2013. Gravity field of the Moon from the Gravity Recovery and Interior Laboratory (GRAIL) mission, *Science*, **339**, 668–671.

APPENDIX A: HARMONIC EXPANSION OF MODE COUPLING TERMS

The terms $\boldsymbol{\mathcal{F}}_D$, $\boldsymbol{\mathcal{B}}_D$, $\mathcal{G}_D$ and $\mathcal{H}_D$, which involve mode coupling between the lateral heterogeneities in material properties and the lower order $(D-1)$ response, exist only in the first and the second order perturbation equations. In order to implement the propagator matrix solution method, we expand those coupling terms into different harmonics that separate into either spheroidal (s) or toroidal (t) mode. Here, we call the lower order response or mode as 'parent' and the modes that result from the coupling as 'child'. A 'child' at a specific mode is indicated by a non-trivial set of expansion coefficients of the coupling terms at that harmonic [eq. (A11) in Qin *et al.* (2014) for VSH expansion]. Assuming that the 'parent', a single eigenstructure of the lateral heterogeneities, and a 'child' are at harmonics (l_0, m_0), (l_1, m_1) and (l, m), respectively, expansion of the coupling terms can be generalized into four categories, depending on whether it is spheroidal or toroidal that the 'parent' and the 'child' belong to.

Following eqs (49) and (51), we divide $F^{x,D}_{lm}$ and $B^{x,D}_{lm}$ further into $\delta\mu_0$, $\delta\lambda_0$ and $\delta\rho_0$ induced terms, as

$$F^{x,D}_{lm} = F^{x,D}_{\mu,lm} + F^{x,D}_{\lambda,lm} + F^{x,D}_{\rho,lm} \tag{A1}$$

and

$$B^{x,D}_{lm} = B^{x,D}_{\mu,lm} + B^{x,D}_{\lambda,lm}, \tag{A2}$$

where x denotes p, b or c component (corresponding to VSH basis functions in eq. (38)). Note that a spheroidal (toroidal) mode does not have c (p or b) component(s). The four categories of expansion coefficients of $\boldsymbol{\mathcal{F}}_D$, $\boldsymbol{\mathcal{B}}_D$, $\mathcal{G}_D$ and $\mathcal{H}_D$ are thus expressed, respectively, as

I) $s(l_0, m_0) \otimes (l_1, m_1) \rightarrow s(l, m)$

i. $\delta\mu_0$ induced:

$$F^{p,D}_{\mu,lm} = \Delta^{\mu}_{l_1 m_1}\mu_0 \left[a_1 \left(\ddot{U} + \frac{2\dot{U}}{r} - \frac{2U}{r^2} \right) + a_2 \frac{V}{r^2} + a_3 \frac{S}{\mu_0 r} \right]^{D-1}_{l_0 m_0}, \tag{A3}$$

$$F^{b,D}_{\mu,lm} = \Delta^{\mu}_{l_1 m_1}\mu_0 \left[a_4 \left(\frac{\dot{S}}{\mu_0} + \frac{3S}{\mu_0 r} \right) + a_5 \frac{U}{r^2} + a_6 \frac{V}{r^2} \right]^{D-1}_{l_0 m_0}, \tag{A4}$$

$$B^{p,D}_{\mu,lm} = \Delta^{\mu}_{l_1 m_1}\mu_0 \left[a_1 \dot{U} \right]^{D-1}_{l_0 m_0}, \tag{A5}$$

$$B^{b,D}_{\mu,lm} = \Delta^{\mu}_{l_1 m_1} \left[a_4 S \right]^{D-1}_{l_0 m_0}, \tag{A6}$$

where $[]^{D-1}_{l_0 m_0}$ means the enclosed r-dependent quantities belong to mode (l_0, m_0) at the order of perturbation $D-1$.

ii. $\delta\lambda_0$ induced:

$$F^{p,D}_{\lambda,lm} = \Delta^{\lambda}_{l_1 m_1}\lambda_0 \left[b_1 \dot{X} \right]^{D-1}_{l_0 m_0}, \tag{A7}$$

$$F^{b,D}_{\lambda,lm} = \Delta^{\lambda}_{l_1m_1}\lambda_0\left[b_2\frac{X}{r}\right]^{D-1}_{l_0m_0}, \tag{A8}$$

$$B^{p,D}_{\lambda,lm} = \Delta^{\lambda}_{l_1m_1}\lambda_0\left[b_1X\right]^{D-1}_{l_0m_0}, \tag{A9}$$

$$B^{b,D}_{\lambda,lm} = 0, \tag{A10}$$

where $X^{D-1}_{l_0m_0} = [\dot{U} + \frac{2U}{r} - \frac{l_0(l_0+1)V}{r}]^{D-1}_{l_0m_0}$.

iii. $\delta\rho_0$ induced:

$$F^{p,D}_{\rho,lm} = \Delta^{\rho}_{l_1m_1}\rho_0\left[c_1(g_0X - \dot{K}) + c_2g_0\frac{V}{r}\right]^{D-1}_{l_0m_0} + f^{p,D}_{\rho,lm}, \tag{A11}$$

$$F^{b,D}_{\rho,lm} = -\Delta^{\rho}_{l_1m_1}\rho_0\left[c_3\frac{K}{r}\right]^{D-1}_{l_0m_0} + f^{b,D}_{\rho,lm}, \tag{A12}$$

where $f^{p,D}_{\rho,lm}$ and $f^{b,D}_{\rho,lm}$ are from the additional terms that depend on the order of perturbation D [eqs (26) and (27)]. When $D = 1$,

$$f^{p,1}_{\rho,lm} = -\Delta^{\rho}_{l_1m_1}\rho_0c_1\dot{\Phi}^{\rm td}_{l_{\rm td},m_{\rm td}} - \delta(l-1, m-m')\rho_0\frac{f_0}{M}, \tag{A13}$$

$$f^{b,1}_{\rho,lm} = -\Delta^{\rho}_{l_1m_1}\rho_0c_3\frac{\Phi^{\rm td}_{l_{\rm td},m_{\rm td}}}{r} - \delta(l-1, m-m')\rho_0\frac{f_0}{M}, \tag{A14}$$

where we assume the tidal potential is at harmonic $(l_{\rm td}, m_{\rm td})$ and thus $V_{\rm td} = \Phi^{\rm td}_{l_{\rm td},m_{\rm td}}Y_{l_{\rm td},m_{\rm td}}$. Here, $\delta(x, y) = 1$ if and only if $x = y = 0$, otherwise $\delta(x, y) = 0$. Therefore, the second terms on the right-hand side of (A13) and (A14) are non-vanishing only when the forcing term $-\delta\rho_0\nabla V_{\rm td}$ causes a degree-1 net force at $(1, m')$ [see eq. (11) for the definition of $\frac{f_0}{M}$]. When $D = 2$,

$$f^{p,2}_{\rho,lm} = -\Delta^{\rho}_{l_1m_1}\rho_0\left\{\delta(l-l'', m-m'')c_1\frac{f_0}{M}\right\}, \tag{A15}$$

$$f^{b,2}_{\rho,lm} = -\Delta^{\rho}_{l_1m_1}\rho_0\left\{\delta(l-l'', m-m'')c_3\frac{f_0}{M}\right\}, \tag{A16}$$

where (l'', m'') is the mode allowed from the coupling of $(1, m')$ and (l_1, m_1) [eq. (27)]. In addition, $\mathcal{G}_D$ and $\mathcal{H}_D$ are caused by $\delta\rho_0$ only, where

$$G^{D}_{lm} = \Delta^{\rho}_{l_1m_1}\rho_0\left[c_1X + c_2\frac{V}{r}\right]^{D-1}_{l_0m_0} \tag{A17}$$

and

$$H^{D}_{lm} = \Delta^{\rho}_{l_1m_1}\rho_0\left[c_1U\right]^{D-1}_{l_0m_0}, \tag{A18}$$

respectively. The constants $a_1, a_2, \ldots, a_6, b_1, b_2, c_1, c_2$ and c_3 are coupling constants and they vary for different couplings.

II) $s(l_0, m_0) \otimes (l_1, m_1) \rightarrow t(l, m)$

i. $\delta\mu_0$ induced:

$$F^{c,D}_{\mu,lm} = \Delta^{\mu}_{l_1m_1}\mu_0\left[a_1\left(\frac{\dot{S}}{\mu_0} + \frac{3S}{\mu_0r}\right) + a_2\frac{V}{r^2}\right]^{D-1}_{l_0m_0}, \tag{A19}$$

$$B^{c,D}_{\mu,lm} = \Delta^{\mu}_{l_1m_1}\left[a_1S\right]^{D-1}_{l_0m_0}. \tag{A20}$$

ii. $\delta\lambda_0$ does not induce toroidal mode, therefore $F^{c,D}_{\lambda,lm} = B^{c,D}_{\lambda,lm} = 0$.

iii. $\delta\rho_0$ induced:

$$F^{c,D}_{\rho,lm} = -\Delta^{\rho}_{l_1m_1}\rho_0\left[c_1\frac{K}{r}\right]^{D-1}_{l_0m_0} + f^{c,D}_{\rho,lm}, \tag{A21}$$

where when $D = 1$

$$f^{c,1}_{\rho,lm} = -\Delta^{\rho}_{l_1 m_1}\rho_0 c_1 \frac{\Phi^{\mathrm{td}}_{L,M}}{r}, \tag{A22}$$

when $D = 2$

$$f^{c,2}_{\rho,lm} = -\Delta^{\rho}_{l_1 m_1}\rho_0 \left\{\delta(l-l'', m-m'')c_1 \frac{f_0}{M}\right\}. \tag{A23}$$

Note that $\mathcal{G}_D$ or $\mathcal{H}_D$ does not appear in the toroidal equations. The coupling constants a_1, a_2, a_3 and c_1 are different from those in the first category.

III) $t(l_0, m_0) \otimes (l_1, m_1) \rightarrow s(l, m)$

i. $\delta\mu_0$ induced:

$$F^{p,D}_{\mu,lm} = \Delta^{\mu}_{l_1 m_1}\mu_0 \left[a_1 \frac{T}{\mu_0 r}\right]^{D-1}_{l_0 m_0}, \tag{A24}$$

$$F^{b,D}_{\mu,lm} = \Delta^{\mu}_{l_1 m_1}\mu_0 \left[a_2\left(\frac{\dot{T}}{\mu_0} + \frac{3T}{\mu_0 r}\right) + a_3 \frac{W}{r^2}\right]^{D-1}_{l_0 m_0}, \tag{A25}$$

$$B^{p,D}_{\mu,lm} = 0, \tag{A26}$$

$$B^{b,D}_{\mu,lm} = \Delta^{\mu}_{l_1 m_1}\left[a_2 T\right]^{D-1}_{l_0 m_0}. \tag{A27}$$

ii. $\delta\rho_0$ induced:

$$F^{p,D}_{\rho,lm} = \Delta^{\rho}_{l_1 m_1}\rho_0 g_0 \left[c_1 \frac{W}{r}\right]^{D-1}_{l_0 m_0}, \tag{A28}$$

$$F^{b,D}_{\rho,lm} = 0. \tag{A29}$$

Note that (A28) and (A29) do not contain extra terms $f^{p,D}_{\rho,lm}$ or $f^{b,D}_{\rho,lm}$.

$$G^{D}_{lm} = \Delta^{\rho}_{l_1 m_1}\rho_0 \left[c_1 \frac{W}{r}\right]^{D-1}_{l_0 m_0}, \tag{A30}$$

$$H^{D}_{lm} = 0. \tag{A31}$$

A toroidal mode will not couple with $\delta\lambda_0$ to induce a 'child' mode.

IV) $t(l_0, m_0) \otimes (l_1, m_1) \rightarrow t(l, m)$

i. $\delta\mu_0$ induced:

$$F^{c,D}_{\mu,lm} = \Delta^{\mu}_{l_1 m_1}\mu_0 \left[a_1\left(\frac{\dot{T}}{\mu_0} + \frac{3T}{\mu_0 r}\right) + a_2 \frac{W}{r^2}\right]^{D-1}_{l_0 m_0}, \tag{A32}$$

$$B^{c,D}_{\mu,lm} = \Delta^{\mu}_{l_1 m_1}\left[a_1 T\right]^{D-1}_{l_0 m_0}. \tag{A33}$$

We find that a toroidal mode coupling with $\delta\rho_0$ does not further induce any toroidal mode, meaning $F^{c,D}_{\rho,lm} = G^{D}_{lm} = H^{D}_{lm} = 0$.

APPENDIX B: SOLUTION PROCEDURE OF PERTURBATION METHOD

The whole solution procedure of the perturbation method is coded up and can be summarized by a flowchart in Fig. B1. At the initial step, the mode of tidal forcing [i.e. (l_0, m_0)], the 1-D reference properties of the planet and the 3-D elastic and density structures (i.e. lateral heterogeneities in eigenstructures, see eqs 39–41) are set up. All quantities are non-dimensionalized. Then, an outer loop solves the mode couplings up to the second order of perturbation for each eigenstructure in the lateral heterogeneities. All the high order response modes and their associated matrix equations are determined, depending on different 'parent'–'child' pairings (see Appendix A). An inner loop then goes through all the response modes and solves for the tidal responses correspondingly, mode by mode, from zeroth to second order of perturbation. The propagator matrix method based on a fourth-order Runge–Kutta numerical scheme is used to solve the matrix equations [appendix C in Qin *et al.* (2014)]. The total tidal response is thus the sum of responses of each mode.

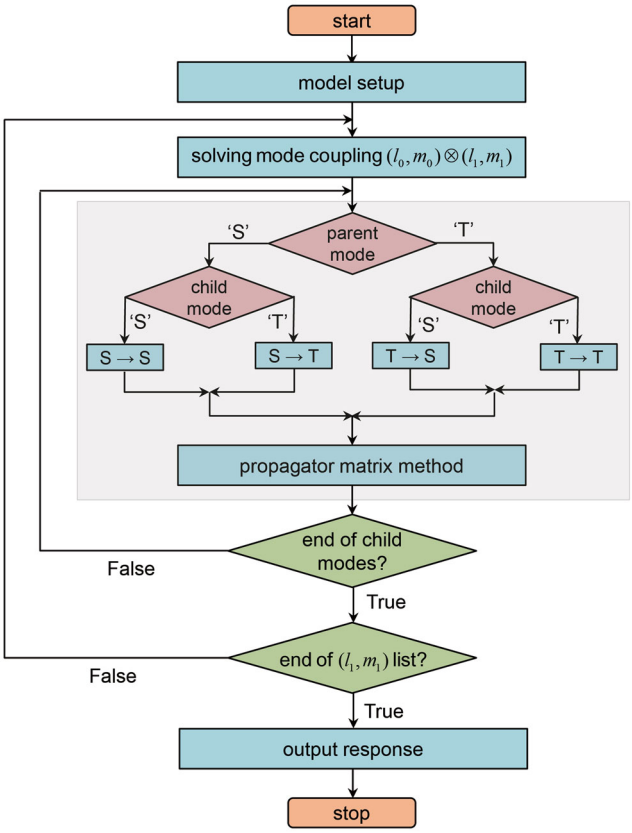

Figure B1. Flowchart of solution procedure of the perturbation method.